Montanuniversität Leoben

High-temperature mechanical testing of novel copper niobium composites

Project report

Mladen-Mateo Primorac

Department of Material Physics, Montanuniversität Leoben, Leoben, Austria

Department for Nuclear Engineering, University of California, Berkeley, USA

Leoben, 15th of August 2013

Index

1 Introduction

The demand of harder, better and more functional materials has stimulated scientists to investigate a new material category – nano-crystalline materials. These materials feature a very small structural size in the order of few nanometer (1 nm = 10^{-9} m). As was reported in many works, this class of materials exhibits extraordinary properties.

One of these promising nano-materials is studied in this work, namely a two phase system composed of the body centred cubic (bcc) element niobium and face centred cubic (fcc) element copper. A phase diagram of the two immiscible elements is shown in Fig. 1.1, whereas only small solubility is shown for copper as well as niobium at elevated temperatures, which diminishes at room temperature. In the last years several investigations were carried out in order to determine the properties of this composite. The copper niobium composite exhibits outstanding performances depending on the amount of niobium in the copper matrix.

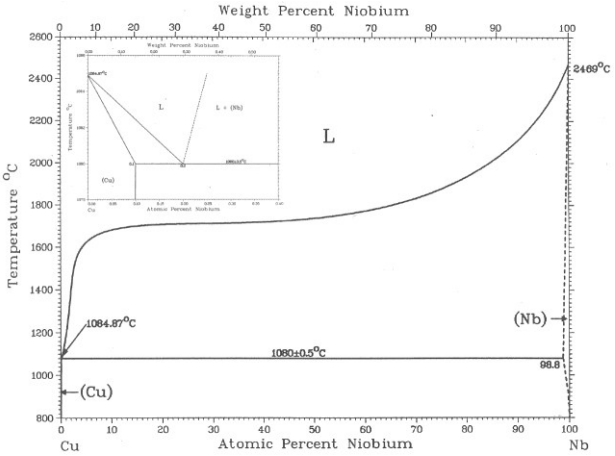

Fig. 1.1: Binary Cu-Nb phase diagram [1].

One of the application areas for copper niobium composites is as ultra high strength conducting materials. According to Botcharova et al. [2, 3, 4] nano-crystalline Cu-Nb alloys exhibit high strength and high conductivity. The insoluble niobium was used in order to strengthen the copper matrix by particle strengthening. The composite was manufactured by mechanical alloying with a maximum niobium content of 20 at.% [2].

Increasing the amount of niobium in the composite to 50 % by a sputtering process for alternating material deposition a nano-layered structure can be achieved, according by Misra, Mara and co-workers [5, 6, 7] as can be seen in Fig. 1.2. The nano-layered structures were sputter deposited with varying layer thicknesses on silica.

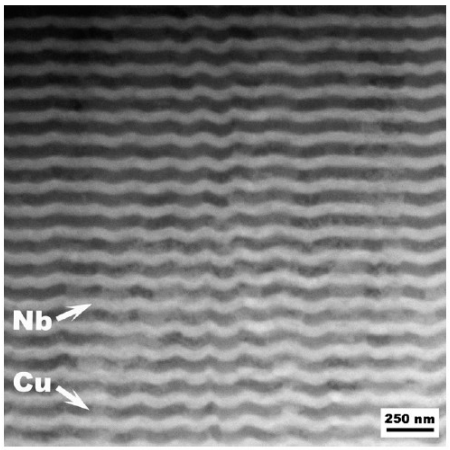

Fig. 1.2: Copper niobium nanoscale multilayers, SEM backscattered electron image [6].

In the work of Misra and co-workers, for example [8, 9], the radiation tolerance after He ion implantation was investigated. The fcc / bcc interface between copper and niobium is favourable for absorbing point defects. Therefore, it was assumed that the nano-composite is favourable as material for application in harsh radiation environments. To maintain the before mentioned properties, the preservation of the nanoscale microstructure at high temperatures (operating temperatures of a reactor are approximately 400 °C) is indispensable.

The aim of this work is to create a novel polycrystalline copper niobium composite for high temperature applications in harsh radiation environments. The material will be manufactured by a severe plastic deformation technique, the high pressure torsion process. Due to the high shear strains that are realized in such a process, a pronounced grain refinement occurs. The microstructure is refined to the sub-micron range. The manufacturing of the specimens, a microstructural characterisation and first microhardness measurements will be realised at the Department of Material Physics at the Montanuniversität Leoben, Austria.

In order to assess the mechanical properties at operating temperatures, the copper niobium composite will be investigated by high-temperature nanoindentation. The high-temperature experiments will be carried out in-situ to obtain the maximum temperature at which the Cu Nb composite can be used. Significant outcomes will be a fundamental understanding of the microstructural stability and the material behaviour at elevated temperatures. Furthermore, the governing deformation mechanisms at elevated temperatures will be investigated. The high-temperature nanoindentation testing will be realised at the Department for Nuclear Engineering at the University of California, Berkeley, United States of America.

2 Theoretical principles

2.1 High pressure torsion

The high pressure torsion (HPT) process is a well-known and recognized process of severe plastic deformation (SPD) and has been studied in various research activities, for example [10, 11, 12, 13]. In the HPT process the material is compacted under a high pressure between two plungers via a hydraulic mechanism [10]; a schematic view is shown in Fig. 2.1. As starting material, for example, bulk materials [11] or powders [12] can be used. In our case the plungers are made of commercial steel. The upper plunger is fixed, while the lower one can perform a torsional rotation with different speed of revolutions per minute. Such rotation is exerted after the compressive pressure is applied. During the HPT process high plastic strains are realized, resulting in fully dense bulk materials with microstructures in the nanocrystalline (nc) and/or ultrafine grained (ufg) size.

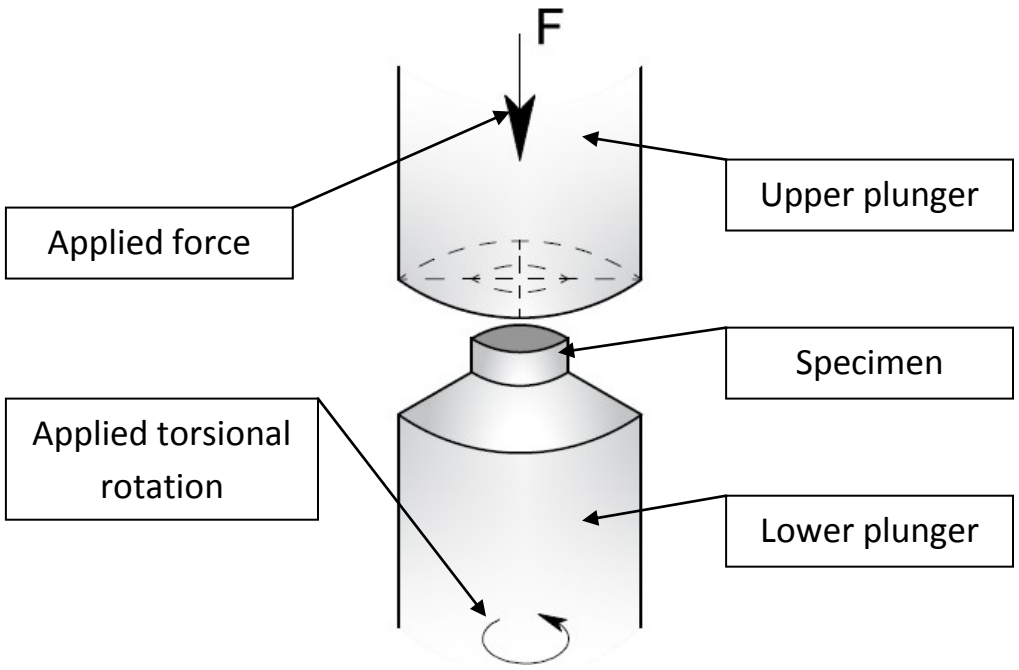

Fig. 2.1: Schematic view of the high pressure torsion process.

However, processing with the HPT approach has also some disadvantages, for example a bimodal distribution of grain sizes and a gradient along the radial as well as in some cases along the axial direction [10]. In order to create a copper niobium composite in the nano-range (nc or ufg range), with the smallest possible gradient along the two axes, two different processing routes were investigated, as will be described later.

2.2 Nanoindentation

A possible way to investigate mechanical properties in small dimensions is achieved by the instrumented indentation technique, also known as “nanoindentation”. The name “nanoindentation” is derived from the small penetration depths ranging in the sub-micron range. In this testing technique the applied load and the resulting penetration depth are recorded in load – displacement curves, as shown schematically in Fig. 2.2. The application area of nanoindentation ranges from thin film testing to highly localized measurements of specified phases in composites as well as in other material classes, e.g. ceramics and polymers [13].

In the last years two different approaches were established to perform high-temperature nanoindentation testing in order to perform highly localized measurements at operating temperatures. The central issue is to minimize the thermal drift between sample and the indenter tip in order to observe repeatable and reliable results. One possibility to measure at higher temperatures is to bring a heatable sample and a non heatable indenter tip in contact and independently wait for thermalisation. The second possibility is to heat the sample and the indenter tip to the same temperature. The thermal drift can be adjusted to a minimum level and thus reliable experiments can be carried out [14].

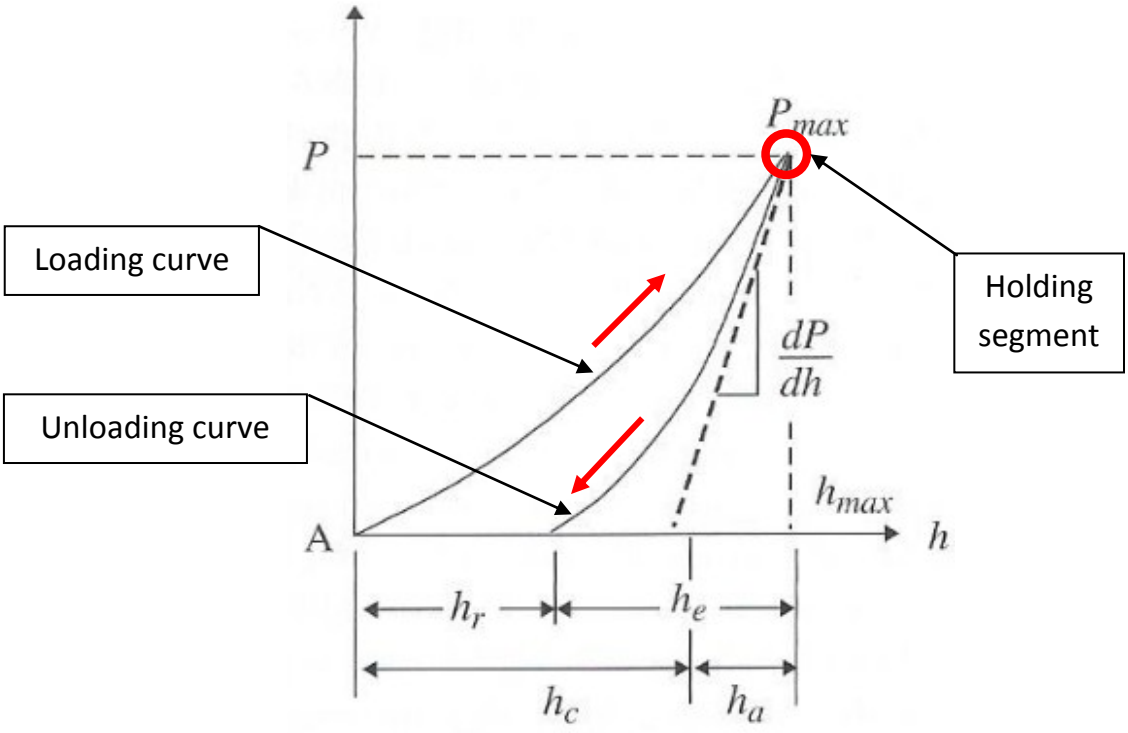

Fig. 2.2: Load – displacement curve as obtained from instrumented indentation testing [10].

The load – displacement curve is the main output of the instrumented indentation technique, and is divided into the loading part (contains elastic and plastic deformation), a hold-

ing segment at maximum load and an unloading part (assumed to be completely elastic). The Oliver-Pharr method is used for the elastic modulus and hardness determination from the unloading curve. A detailed explanation of this method will not be given in this work, but can be found for example in [13, 14]. Nonetheless, a brief description is summarized in the following part. According to equation 2.1 the hardness (H) of the material can be determined by dividing the maximum load (P_{max}) by the contact area (A_{c}).

$$H = \frac{P_{\mathrm{max}}}{A_{\mathrm{c}}} \qquad \text{(Eq. 2.1)}$$

The contact area (A_{c}) and the indentation depth (h_{c}) are calculated by the tip area function (equation 2.2) and determined by the geometry of the indenter. For an idealized Berkovich indentation tip geometry the parameter a_0 equals 24.5. With progressing time and use of the indenter, the tip gets more rounded resulting in a different tip geometry, which has to be accounted for as outlined below.

$$A_{\mathrm{c}} = a_0 \cdot h^2 \qquad \text{(Eq. 2.2)}$$

In order to avoid errors in the measurement, a calibration has to be carried out on an isotropic sample with known properties – elastic modulus and Poisson's ratio. A fused silica calibrating sample was used as reference material to calibrate the tip area function and to determine the fit parameters *a*, *b* and *c* of equation 2.3. The parameter *a* is usually close to 24.5, the parameter *b* reflects the tip rounding from the ideal shape. It has to be mentioned that also other functions are commonly used, as described in [13, 14].

$$A(h_{\mathrm{c}}) = a \cdot {h_{\mathrm{c}}}^2 + b \cdot h_{\mathrm{c}} + c \qquad \text{(Eq. 2.3)}$$

Furthermore, an analytical determination of the Young's modulus is possible, when considering A_{c} and the contact stiffness (S), as well as the geometry factor (β), which in the case of a Berkovich indenter is 1.034. According to equation 2.4 the reduced modulus (E_r) of the sample can be determined, which reflects the combined modulus of sample and tip.

$$E_r = \frac{\sqrt{\pi}}{2 \cdot \beta} \cdot \frac{S}{\sqrt{A}} \quad \text{(Eq. 2.4)}$$

With this reduced modulus and equation 2.5 the Young's modulus of the sample (E_s) can be determined. The required parameters are the Poisson's ratio of the sample (ν_s) and the properties of the indenter (ν_i and E_i).

$$\frac{1}{E_r} = \frac{(1-\nu_s{}^2)}{E_s} + \frac{(1-\nu_i{}^2)}{E_i} \quad \text{(Eq. 2.5)}$$

The measurement of further mechanical properties, for example fracture toughness, residual stress and the strain hardening index (the inverse of the strain rate sensitivity), with nanoindentation techniques is possible [13]. Several techniques have been investigated to measure the strain rate sensitivity (SRS), also referred to as m-value, with nanoindentation. The SRS is described by equation 2.6, as the ratio of the natural logarithmic hardness and the natural logarithmic strain rate, whereat the temperature has to be kept constant.

$$m = \left(\frac{\partial \ln(\sigma)}{\partial \ln(\dot{\varepsilon})}\right)_T \approx \left(\frac{\partial \ln(H)}{\partial \ln(\dot{\varepsilon})}\right)_T \quad \text{(Eq. 2.6)}$$

The hardness is calculated by equation 2.1; the strain rate is determined as the ratio of the displacement rate ($\dot{h}$) to the displacement (h), as can be seen from equation 2.7.

$$\dot{\varepsilon} = \frac{\dot{h}}{h} \quad \text{(Eq. 2.7)}$$

The most promising methods to ascertain the strain rate sensitivity are the constant rate of loading (CRL) method proposed by Mayo and Nix [15], the strain rate jump tests reported in [16, 17], the constant strain rate (CSR) method suggested by Lucas and Oliver [18, 19], and the constant load (CL) method recommended by Mayo et al. [20, 21].

The methods that can be carried out on the nanoindentation facility used in this work are the CSR and the CL method, and thus will be discussed next. To obtain SRS values from CSR measurements, hardness and strain rate pairs are needed over minimum two orders of magnitude on the strain rate axis, as can be seen in Fig. 2.3 in order to have meaningful results [14]. During a CSR measurement the strain rate of the loading is kept constant, which is realised by an exponential loading segment. The strain rate is adjusted by a proportional constant (k) that shows the ratio from the loading rate ($\dot{P}$) to the applied load (P). The strain rate results from the constant k divided by the factor two.

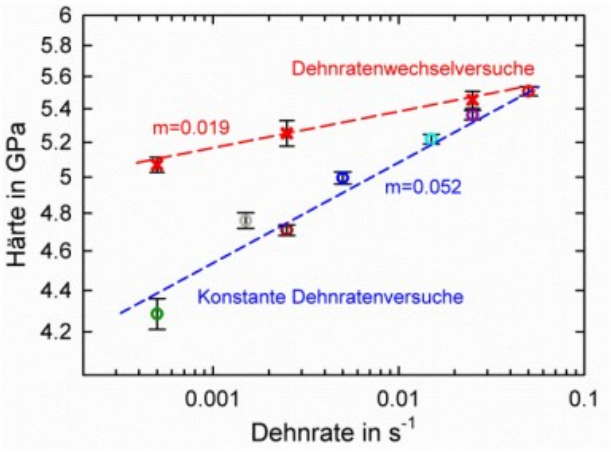

Fig. 2.3: Hardness – strain rate diagram: strain rate jump tests (red curve) compared to constant strain rate tests (blue curve) showing higher values for CSR results for nc nickel [14].

Fig. 2.3 implicates that higher strain rate sensitivity values are observed in the CSR method (blue curve) than for strain rate jump tests (red curve) in the case of nano-crystalline nickel [14]. The disadvantage of the CSR method is the high amount of indents necessary for a statistical analysis of the obtained data.

The second method to measure the SRS is the CL method. According to Mayo et al. and Peykov et al. [15, 22] for the CL method less indents are needed, resulting in a smaller required area on the sample, due to the fact that only one indent with a constant load is needed. The SRS values from the CL method are obtained from the holding segment at maximum load (dwell period of 100 seconds) [22]. According to Peykov et al. a graph with *constantly changing strain rate and hardness pairs* is used to calculate the SRS. The curve is then divided into two different stages. Peykov et al. indicated the two stages to “Stage I” and “Stage II” (Fig. 2.4). The CL method will be discussed in chapter 4.3.4 more in detail.

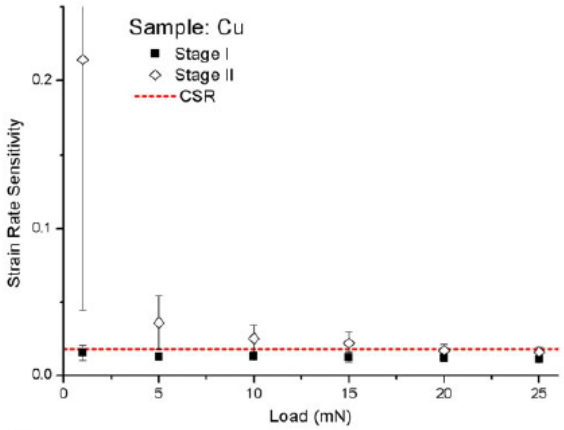

Fig. 2.4: Comparison of the CSR and the CL method for bulk copper, whereat CSR results and CL "Stage I" measurements exhibit nearly the same SRS [22].

Furthermore, Peykov et al. reported a good agreement between the results obtained from constant strain rate measurements (red dotted line) and the findings of "Stage I" from constant load tests (black squares). The data from "Stage II" exhibits higher SRS values [22].

A second parameter for determining the governing deformation mechanism, the activation volume of the process governing plastic flow (V^*), can be calculated according to equation 2.8. The activation volume is an indicator for the deformation dynamics. The required parameters are the Boltzmann constant (k_B) and the absolute temperature (T).

$$V^* = \sqrt{3} \cdot k_B T \cdot \left(\frac{\partial \ln(\dot{\varepsilon})}{\partial \sigma}\right)_T \qquad \text{(Eq. 2.8)}$$

In order to illustrate this value it is often divided by the atomic volume, which is assumed to be the cubed Burger's vector (b) b^3, giving a measure of the number of unit cells involved in the rate limiting step for plastic deformation.

3 Materials and Methods

3.1 Sample preparation

The material investigated in this work was obtained by several processing steps. In the beginning a commercial copper powder (99.9 % purity, particle size in the range from 40 to 80 µm) and a niobium powder (99.8 % purity, particle size smaller than 45 µm) were put together and mixed at room temperature for 60 minutes. The micrometer-sized powder mixture contained equal amounts of both powders, respectively 15 g, resulting in a composition with 50 wt.% copper and 50 wt.% niobium. The atomic percentage is 41 at.% niobium and 59 at.% copper, whereas the volume percentage is 49 vol.% copper and 51 vol.% niobium.

After the mixing of the two powders it was necessary to create a fully dense bulk material with a microstructure in the nano-crystalline (nc) or ultrafine grained (ufg) range. To create such a composite with a fine microstructure in the order of 100 nm from the powder mixture the high pressure torsion (HPT) technique was used.

3.2 High Pressure Torsion

The HPT process was performed on two HPT machines. The “small” HPT machine has a maximum pressure of 40 tons, where two plungers measuring 40 mm in diameter were used, as shown in Fig. 3.1. The specimen received is disk-shaped, measuring approximately 8 mm in diameter and 0.6 mm in height.

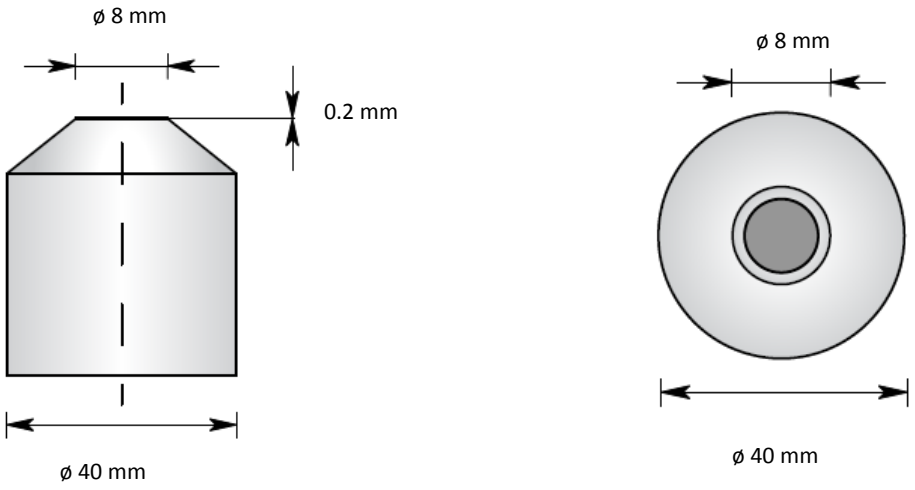

Fig. 3.1: Schematic view and dimensions of the plungers from the “small” HPT tool.

The “large” HPT machine has a higher nominal pressure of 400 tons. The two plungers are also bigger compared to the small one, measuring 150 mm in diameter (Fig. 3.2). The specimen geometry is nearly the same as in the other case, but again with larger dimensions. The obtained sample measures around 35 mm in diameter and 7 mm in height.

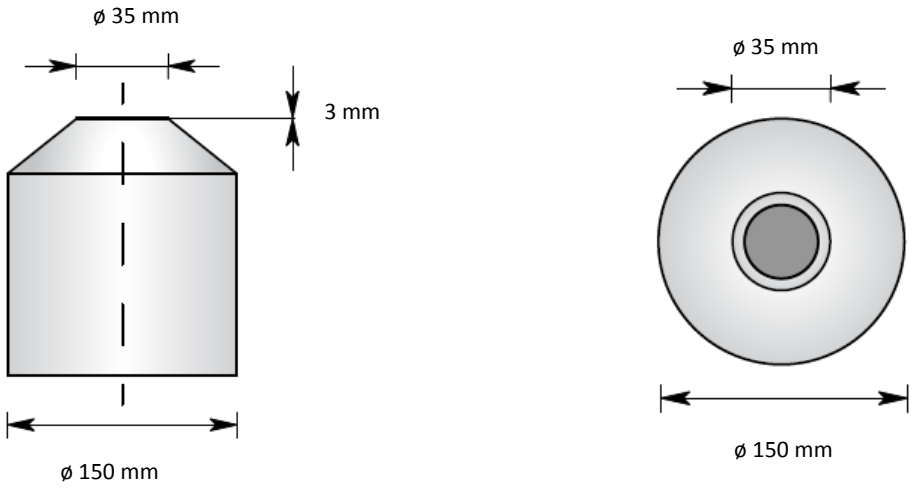

Fig. 3.2: Schematic view and dimensions of the plungers from the “large” HPT device.

3.2.1 One step HPT process

One of the two processing routes is the commonly used “one step” HPT process, as above described and often mentioned in literature. In order to retain the powder in the right position for the HPT process, a copper ring was positioned on the lower plunger measuring approximately 8.5 mm in diameter and 2.5 mm in height and filled with the powder mixture subsequently. The samples were fabricated with the “small” HPT tool, where the number of revolutions was varied from 60 to 200 to ascertain a possibly fine and saturated microstructure evolution. After the deformation all disk-shaped samples measured approximately 8 mm in diameter and 0.6 mm in height, as can be seen schematically in Fig. 3.3.

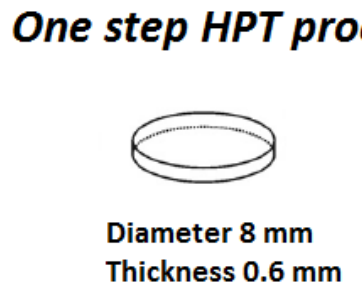

Fig. 3.3: Schematic view of the sample disks obtained from the “one step” HPT process.

3.2.2 Two step HPT process

A second possible processing route to obtain materials with a microstructure in the nano-range is the so called “two step” HPT process. According to Bachmeier et al. [12], a two step HPT process should implicate a more homogenous microstructure and furthermore smaller grain sizes. This two step process starts with pre-compacting of the copper niobium powder mixture in the “large” HPT machine, again using an outer ring for filling the powders. The rotational speed was set to 0.067 rpm, the pressure to approximately 200 bar. After ten revolutions a 7 mm high disk, measuring 35 mm in diameter was obtained – the first deformation step was completed. The disk exhibited in the outer regions a macroscopic difference in microstructure compared to the inner regions; this arises from the copper-silver ring that was used to avoid flow of the powder mixture.

From the disk-shaped sample two rods with a diameter of 7 mm were machined. Subsequently, smaller disks (7 mm diameter, 1.1 mm height) were cut out of the rods and put into the “small” HPT machine for a second deformation step. This procedure is shown in Fig. 3.4.

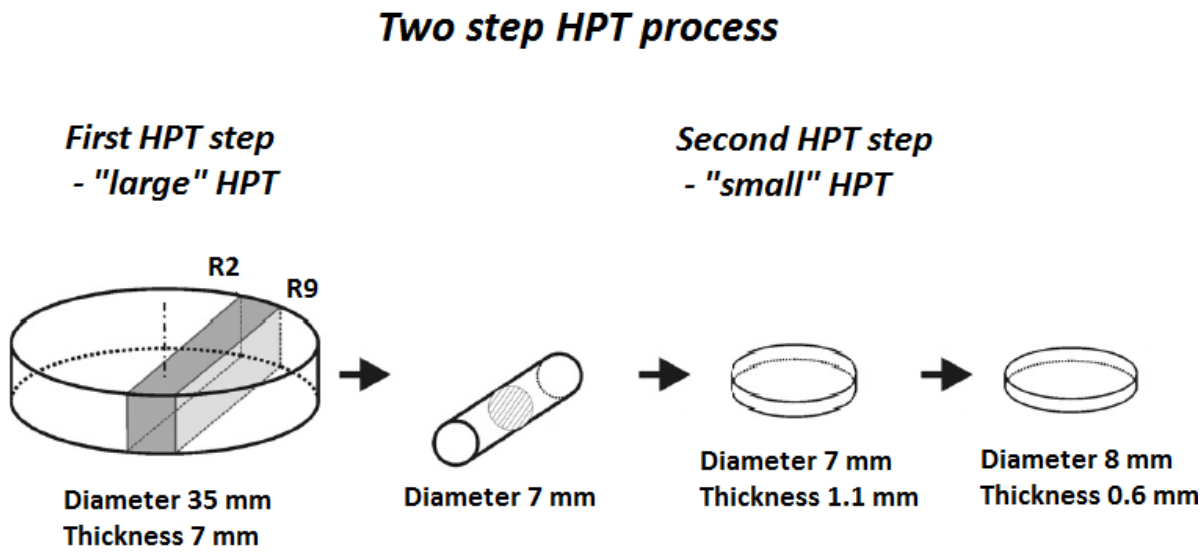

Fig. 3.4: Schematic view of the “two step” HPT process, adapted from [12].

The disks were deformed in perpendicular deformation direction to the first processing step to break down the so-called deformation striations, which are often observed during HPT deformation. In order to investigate the best possible processing, the number of revolutions was varied from 100 to 200. After the second deformation step the specimens had approximately the same diameter as in the “one step” HPT process. The height of the disks were slightly lower, approximately 0.5 to 0.6 mm.

3.3 Heat treatment

In different former investigations copper niobium composites in the nc range exhibited high thermal stability during annealing at elevated temperatures. For example, Botcharova et al., discovered a high thermal stability of mechanically-alloyed nc copper niobium alloys with (microstructure size of 50 nm) after annealing for 10 hours at 1000 °C [4]. On the other hand, Misra et al. reported in their research study dealing with nano-layered copper niobium thin films (microstructure size of 75 nm) a temperature stability for long annealing times at 700 °C [5]. In order to ensure a fine grained microstructure that is necessary for the demanded properties of the novel copper niobium composite, a thermal stability check is indispensable.

With a view to the structural stability at elevated temperatures of the nc / ufg copper niobium composite, which among other things is investigated in this work, a heat treatment was carried out. Beyond that, the annealing is necessary to avoid (saturated) solid solutions, although copper and niobium are immiscible. Previous investigations showed that even immiscible elements can form saturated solutions, according to Bachmeier et al. [12], due to mechanical intermixing during HPT processing. The samples were heated in a XERION vacuum furnace at 500 °C for 60 minutes. During the whole heat treatment (heating, holding, cooling) the furnace was consistently under a vacuum of $3 \cdot 10^{-4}$ mbar. The temperature profile is shown in Fig. 3.5, whereat the heating rate is pointed out. The cooling was carried out without a preset cooling rate.

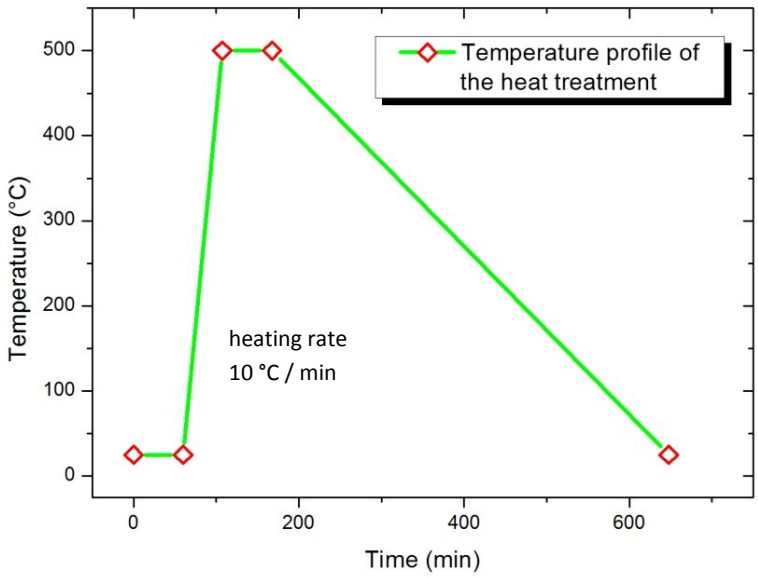

Fig. 3.5: Temperature profile of the heat treatment of the copper niobium composites processed by the HPT technique.

The first holding segment in Fig. 3.5 is for establishing the vacuum; the heating rate of 10 °C per minute was adjusted. After the heat treatment at 500 °C the specimens were slowly cooled in the vacuum furnace to room temperature without a specific cooling rate.

3.4 Microindentation hardness testing

In order to assess the homogeneity of the produced samples and an estimation of the strength of the composite after the different HPT processes, microhardness measurements were carried out. The aim was to investigate the homogeneity in the x-axes (tangential deformation direction – radial direction of the sample). The measurements were made on a BUEHLER Micromet 5100 using a diamond Vickers indenter. The testing load was set to 500 gf, resulting in an indent size in the range from 40 to 60 µm, depending on the radial position, respectively the material hardness. A distance between each indent of 250 µm was kept constantly along the x-axes to avoid any interaction between deformed volumes.

3.5 Microstructural characterization

To examine the microstructure of the novel copper niobium composite with microscopic methods, the samples were embedded on a STRUERS ProntoPress-10 in PolyFast, a phenolic hot mounting resin with carbon fillers, at 180 °C and a load of 15 kN. The process time was 15 minutes. After the embedding the samples were prepared by a metallographic procedure on a STRUERS TegraPol-11. The schedule for the grinding and polishing is given in Table 3.1.

Table 3.1: Standard metallographic grinding and polishing procedure.

Disk type	Name		Duration
Grinding disk	Piano	Planar grinding	1 minute
Grinding disk	Largo	1200	4 minutes
Polishing disk	Dac	3 µm	3 minutes
Polishing disk	Nap	1 µm	2 minutes
Polishing disk	Chem	OPS	2 minutes

For the characterization by different microscopic techniques the samples were etched for 10 seconds to increase the contrast. The wet etchant consisted of ethanol, iron(III)-chlorid and hydrochloric acid and is usually used for etching copper samples. The exact composition can be seen in Table 3.2.

Table 3.2: Composition of the wet etchant for copper.

Name	Chemical symbol	Amount	Unit
Ethanol	C_2H_6O	100	ml
Hydrochloric acid	HCl	20	ml
Iron(III)-chlorid	$FeCl_3$	5	g

The microstructural characterization was carried out with a light-optical microscope (LOM) and a scanning electron microscope (SEM) type LEO 1525 using a back-scatter detector. A general light optical microscopic overview was realized in radial direction with a magnification of 100x. The samples were examined in radial direction in the SEM, too. The operating voltage was set to 20 kV, the working distance to 6.4 mm.

3.6 Nanoindentation hardness testing

3.6.1 Experimental setup

To investigate mechanical properties of the novel copper niobium composite in the submicron range as well as time dependent properties depth sensitive indentation – "nanoindentation" – was used. The measurements were performed on a Micro Materials facility shown in Figure 3.6 (a). Furthermore, this nanoindenter offers the possibility to perform high temperature measurements to a maximal temperature of 700 °C. This is achieved by heating the sample as well as the indenter tip to avoid thermal drift. With this nanoindenter in-situ high temperature mechanical properties can be measured. A high temperature setup can be seen in Figure 3.6 (b).

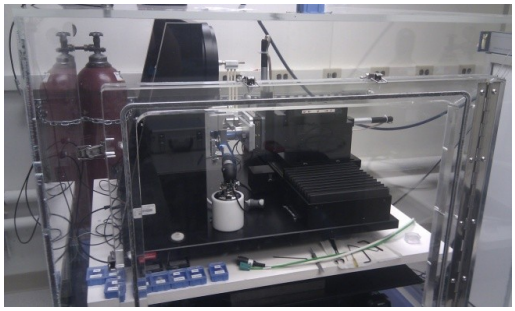

Fig. 3.6 (a): Overview of the Micro Materials nanoindentation facility with the pumping chamber.

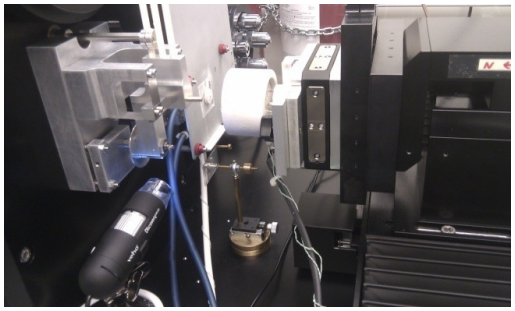

Fig. 3.6 (b): High-temperature setup of the Micro Materials nanoindenter.

In Fig. 3.6 (a) a chamber and gas bottles in the background are visible. The chamber, and hence the nanoindentation experiment, can be purged with gas to bring the oxygen content in the chamber to < 1%, although oxidation cannot be totally avoided. A more detailed view of the high temperature sample holder ("hot stage") and the heatable indenter tip can be seen in Fig. 3.7. In order to figure out the optimal measurement position for the indentation tests, a microscope is installed. The heat shield serves as a thermal protection for the connecting wires of the indenter tip. In order to measure at higher temperatures, a water cooling system is indispensable.

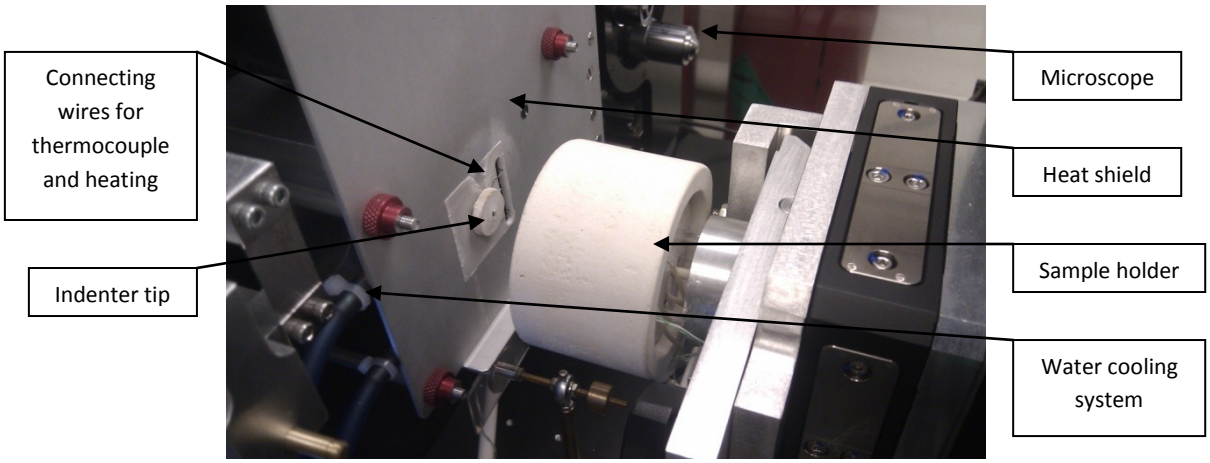

Fig. 3.7: Detailed view of the high-temperature setup; the indenter tip and the hot stage, as well as other features as listed above are apparent.

The used indenter tips were a diamond Berkovich indenter for the measurements at room temperature and a heatable cubic boron nitride (cBN) Berkovich indenter for the high temperature experiments. The heatable cBN indenter can be used to a maximum temperature of approximately 700 °C. The area function of the indenter was calibrated before and after an experimental run at elevated temperatures in order to minimize the influencing factors from tip wearing.

The analysing software is called Nano-Test Platform Three from Micro Materials.

3.6.2 Sample preparation for nanoindentation

The HPT samples were grinded to half of the height, i.e. approximately 250 to 300 µm. This was achieved by measuring the thickness of the sample (height) every 20 seconds while grinding. Afterwards the disks were polished with the same procedure as described in Table 3.1 from chapter 3.5.

To perform the instrumented indentation testing the polished samples were mounted on two different sample holders, depending at which temperatures the measurements should be carried out. In the case of room temperature measurements, the polished disks were mounted with common super glue on steel sample holders.

In the case of high temperature measurements, the polished specimens were mounted with high temperature cement on the hot stage sample holder as can be seen in Figure 3.8. In order to measure the surface temperature of the specimen during the heat treatment, a thermocouple was attached to a second identical sample (*temperature reference sample*) that was mounted right beside the testing sample. This second sample, as well as the thermocouple wires, was fully covered with the high temperature cement.

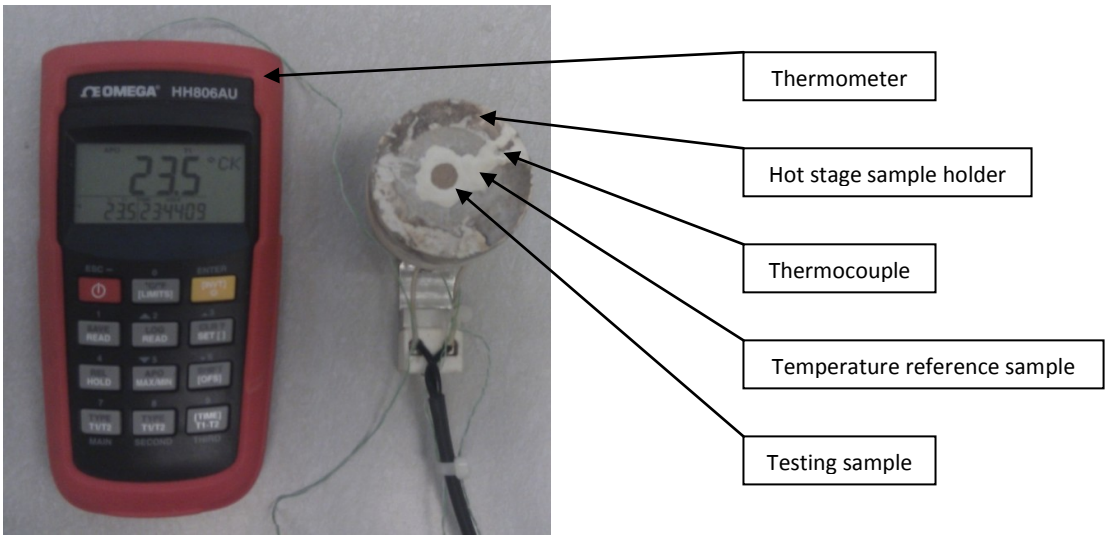

Fig. 3.8: Thermometer, thermocouple and mounted sample on the “hot stage”.

The mounting of the testing sample was difficult due to the fact that a disk-shaped HPT sample is not fully flat on the opposite side (non polished side). Because of this, a thin layer of cement was put under the sample to ensure planarity to the hot stage sample holder. A usual drying of the cement lasts for approximately 24 hours. By heating up the sample on the hot stage to 60 °C for 60 minutes this drying process could be accelerated. Simultaneously, the function of the thermocouple was tested.

The nanoindentation measurements were performed load controlled and depth controlled, whereas the vast majority of the experiments were carried out load controlled. The tests had the following parameters shown in Table 3.3 in common. A few other parameters had to be changed depending on which method has been used.

Table 3.3: General testing parameters for nanoindentation testing.

Parameter	Unit	Value
Limit Stop Load	mN	0.10
Indenter Contact Velocity	µm/s	0.50
Initial Load	mN	0.10
Dwell Period for Drift Correction	s	60

In the case of the load controlled method, the ramp type was set to “fixed time”. Further particulars can be seen in Table 3.4. All load controlled measurements, unless otherwise noted, feature the mentioned parameters and vary only in the duration of the dwell period.

Table 3.4: Loading and unloading parameters of load controlled measurements.

Parameter	Unit	“Fixed time”
Load Time	s	10
Unload Time	s	5

In the case of the depth controlled method, the ramp type was once set to “fixed rate” and the other time to “proportional”. The particulars for the first ramp type as well as the second ramp type are shown in Table 3.5. The “proportional” tests were used to perform the CSR measurements. The depth controlled measurements were performed using the shown parameters unless otherwise noted.

Table 3.5: Loading and unloading parameters of depth controlled measurements.

Parameter	Unit	“Fixed rate”	“Proportional”
Loading Rate	mN/s	10	-
Unloading Rate	mN/s	20	20
Proportional Constant	1/s	-	0.10

A distance of 30 µm was kept constant between the indents to avoid an overlapping of the plastic zones and thus an influence between two adjacent indents. In order to determine the high temperature mechanical properties two experimental runs were performed on nominally identical specimens; one starting from room temperature to a maximum temperature of 300 °C, and the second starting from 300 °C to a maximum temperature of 500 °C.

The temperature profile of the first run is shown in Fig. 3.9 (a), the profile of the second one can be seen in Fig. 3.9 (b). The red squares mark the beginning point, the thermalisation point and the end point of each segment. The heating rate is 1.6 K/s.

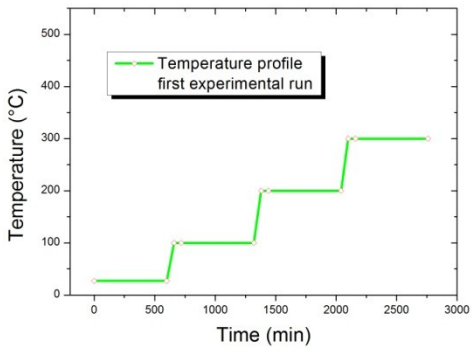

Fig. 3.9 (a): Temperature profile of the first experimental run (from RT to 300 °C).

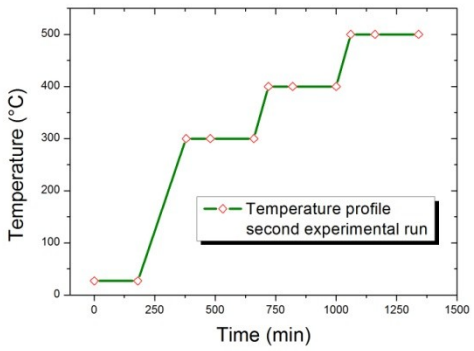

Fig. 3.9 (b): Temperature profile of the second experimental run (300 °C to 500 °C).

As can be seen from Fig. 3.9 (a) and Fig. 3.9 (b) experiments were performed every 100 °C. In the first experimental run the sample was exposed for around 600 minutes at the testing temperature, due to the fact that five different indent settings (two load controlled and three depth controlled sets) were performed. Each setting consists of ten indents, resulting in an array ("indent field") of approximately 120 µm times 270 µm (Fig. 3.10).

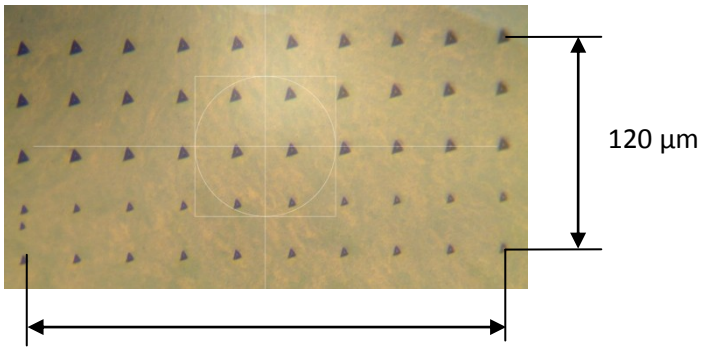

Fig. 3.10: Indent field area showing three depth controlled and two load controlled test runs from room temperature measurements.

In the second experimental run the holding segment takes approximately 300 minutes at each testing temperature. This is due to the fact that two different indent settings (two load controlled measurements) were performed. As described in the first run, each setting consists of ten indents, resulting in a smaller array size of 30 µm times 270 µm.

4 Results and Discussion

4.1 Microindentation hardness testing

4.1.1 First microhardness testing

The first microhardness measurements were performed on three specimens, each of them representing a different processing set. The two processing routes (“one step” and “two step” HPT deformation) as well as a different number of revolutions in the “one step” process were investigated. The three processing categories are shown in Table 4.1.

Tab. 4.1: Investigated HPT processing routes.

Sample number	Processing route	Characteristic
#1	“one step” HPT	60 revolutions
#2	“one step” HPT	150 revolutions
#3	“two step” HPT	200 revolutions

The first sample number #1 represents a low number of revolutions. The microindentation testing was performed along the whole x-axes on the full length of the sample (black curve). In Figure 4.1 the microhardness values are shown.

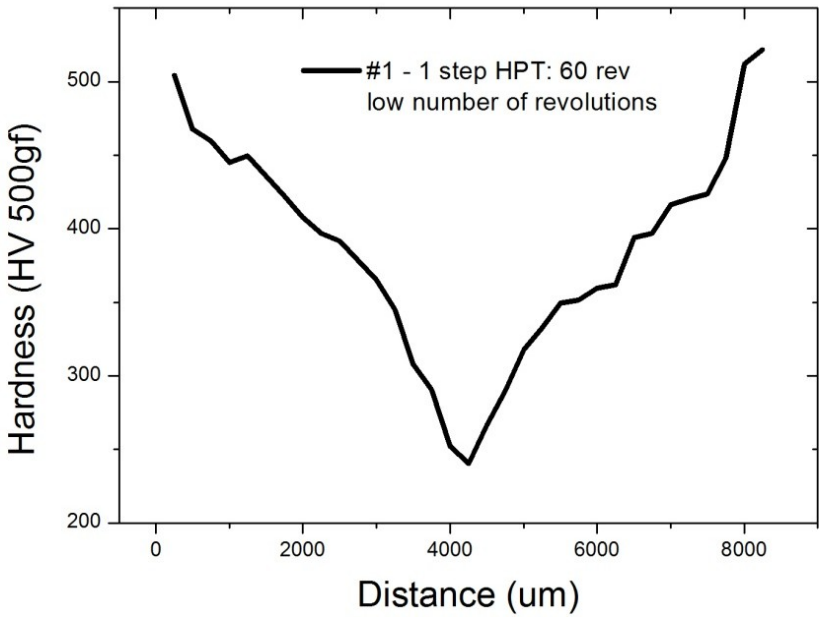

Fig. 4.1: Microhardness measurements of sample #1 over the whole radial direction.

In the outer regions – were the highest plastic strain is realized – the hardness values are higher than in the inner regions of the sample where lower plastic strain occurs. This phenomenon is often obtained when hardness measurements are performed on HPT samples and is a consequence of equation 4.1 [23]. The equivalent strain (ε_{eq}) describes the introduced strain as a function of the number of revolutions (n), the radial position - radius (R) and the thickness of the sample (t).

$$\varepsilon_{eq} = \frac{2 \cdot \pi \cdot n \cdot R}{\sqrt{3} \cdot t} \qquad \text{(Eq. 4.1)}$$

An equivalent strain at radius R = 3 mm was calculated to be approximately ε_{eq} = 1100 for this sample.

4.1.2 Second microhardness testing

Because of the symmetric behaviour of the hardness values, further microhardness measurements were performed from the centre point of the specimen to the edge of the sample over a distance of 4 mm. In Figure 4.2 the results of microindentation testing for all three processing routes are compared.

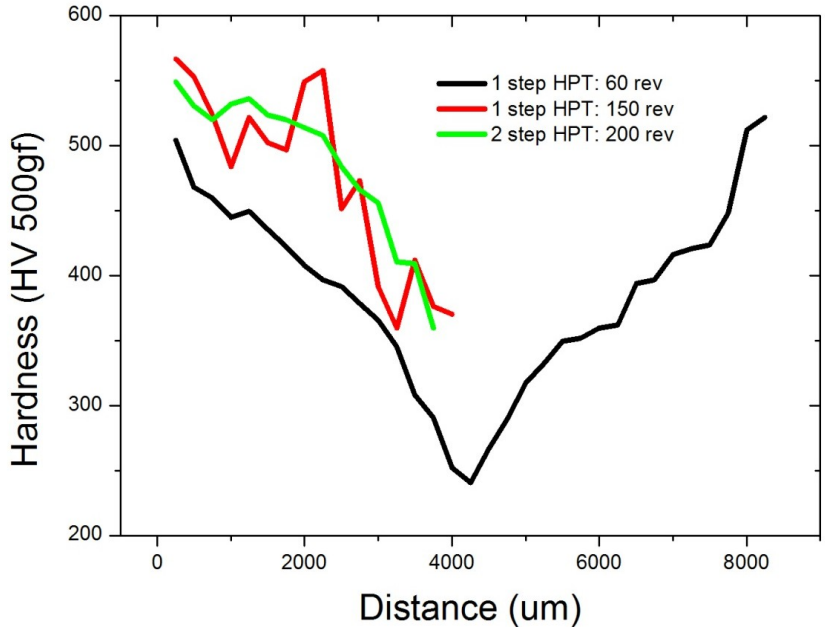

Fig. 4.2: Comparison of the microhardness results obtained from sample #1 (black curve), sample #2 (red curve) and sample #3 (green curve), showing the influence of the processing on the achieved hardness.

The graphic shows higher hardness values for the samples which were prepared using a HPT process with a high number of revolutions. A difference of approximately 50 HV (or more than 10% of the absolute hardness values) is observed between low and high number of revolutions. In literature it is often shown that a finer microstructure, hence higher hardness values, are expected with higher number of revolutions, for example according to [11].

Furthermore the two processing routes are slightly different. While the sample obtained from the “one step” HPT process (red curve) shows more variation over the radial direction, the hardness values of the “two step” HPT sample (green curve) are more constant along the x-axes. In case of the “two step” HPT process the microstructure is much finer than in the “one step” processing route, resulting in a higher hardness. This correlates with the work from Bachmeier et al. [12].

4.1.3 Influence of the heat treatment

In order to determine the influence of the heat treatment on the microstructure, the micro-hardness of non heat treated samples, as well as heat treated samples, was measured after annealing at 500 °C for 60 minutes. The heat treatment was only carried out on the samples with a high number of revolutions, due to the fact that sample number #2 and sample number #3 showed higher hardness values in the first microhardness measurements compared to sample number #1.

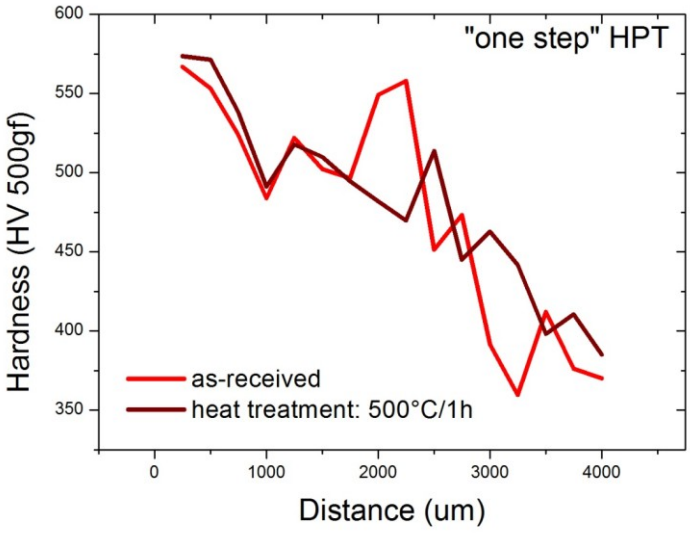

Fig. 4.3: Microhardness measurements of sample #2 – non heat treated (red curve) and heat treated at 500 °C for 60 minutes (dark red curve).

Fig. 4.3 shows the microhardness data obtained from the non heat treated (red curves) and the heat treated (dark red curves) “one step” sample. A slight reduction in the variation of the data is observed, although an area of constant values is not obtained.

In Fig. 4.4 the hardness values of the non heat treated (green curve) and the heat treated (dark green curve) “two step” sample is shown. A constant plateau in the range around 1.0 mm can be seen. The microhardness values in this area are approximately 525 HV.

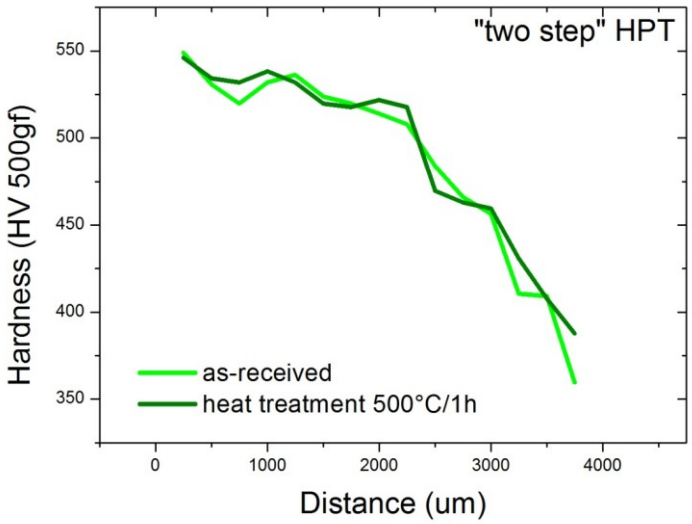

Fig. 4.4: Microhardness measurements of sample #3 – non heat treated (green curve) and heat treated at 500 °C for 60 minutes (dark green curve).

In total, microhardness measurements in radial directions were performed on five specimens shown in Table 4.2. Each of them represents a different processing technique.

Tab. 4.2: Overview of samples tested by microhardness measurements.

Sample number	Processing route	Number of revolutions	Heat treatment
# 1	“one step” HPT	60	-
# 2	“one step” HPT	150	-
# 2 ht	“one step” HPT	150	500 °C for 60 min
# 3	“two step” HPT	10 (1st step), 200 (2nd step)	-
# 3 ht	“two step” HPT	10 (1st step), 200 (2nd step)	500 °C for 60 min

Higher hardness values are obtained for the samples which were prepared by a high number of revolutions. The “two step” HPT process showed higher hardness values compared to a

“one step” HPT process with low number of revolutions and more constant hardness values compared to the “one step” HPT process with high number of revolutions.

4.2 Microstructural characterization

4.2.1 Light-optical microscopy

In order to obtain a first overview of the copper niobium composites processed by different processing routes and investigated in this work, a microstructural characterization was performed with a light-optical microscope (LOM) subsequently to microhardness measurements. The indents from the micro-indentation testing are apparent in all LOM pictures. Each sample was examined along the whole radial direction.

“One step” HPT: Sample #1

In Fig. 4.5 a cross section of a whole disk-shaped HPT sample is shown. From one end to the other the disk measures 8 mm. The middle of the sample is pointed out and labelled with R_0. This represents the centre point of the HPT sample R_0 = 0.0 mm. A detailed view was carried out from radius R_1 = 2.5 mm to a radius R_2 = 3.5 mm, due to the fact that the hardness values from microhardness indentation testing in this region showed the highest values. Furthermore in this region the finest microstructure is assumed. The outer regions of the sample (R > 3.5 mm) were declared as saturation region and were not included for microstructural characterization.

Fig. 4.5: Cross section of a HPT sample in the light optical microscope.

Due to the similarity of the disk-shaped samples along the radial direction, the microhardness was determined only on one half of the sample (Fig. 4.1). Because of that the microstructural characterization was also performed only on one half of the specimens (Fig. 4.6). The detailed view is indicated by a rectangle in Fig. 4.7.

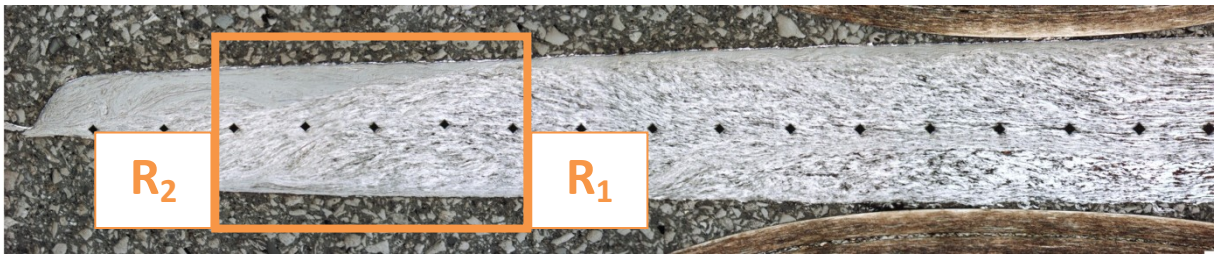

Fig. 4.6: Profile of sample #1, showing half of the HPT sample with microhardness indents.


Fig. 4.7: Detailed view from R_1 = 2.5 mm to R_2 = 3.5 mm of the profile of sample #1.

In Fig. 4.7 the microstructure of sample #1 is shown. On outer regions of the disk-shaped sample saturation regions can be seen (grey areas), whereas in the middle of the sample white and black areas are present. The white and black areas can be related to copper and niobium. The microstructure is coarse due to the fact that it is resolvable with light-optic microscopy and a hundredfold (100x) magnification.

“One step” HPT: Sample #2

Fig. 4.8: Profile of sample #2, showing half of the HPT sample with microhardness indents.

Fig. 4.8 and Fig. 4.9 show sample number #2. Compared to sample #1 a finer microstructure is observed as indicative by more featureless areas. In contrast to the first impressions these ones show more deformation striations, resulting in a lower homogeneity than sample #1. In Fig. 4.8 micro-cracks are visible at approximately R = 2.0 mm. These cracks result from the high plastic strains that are induced during the HPT process.

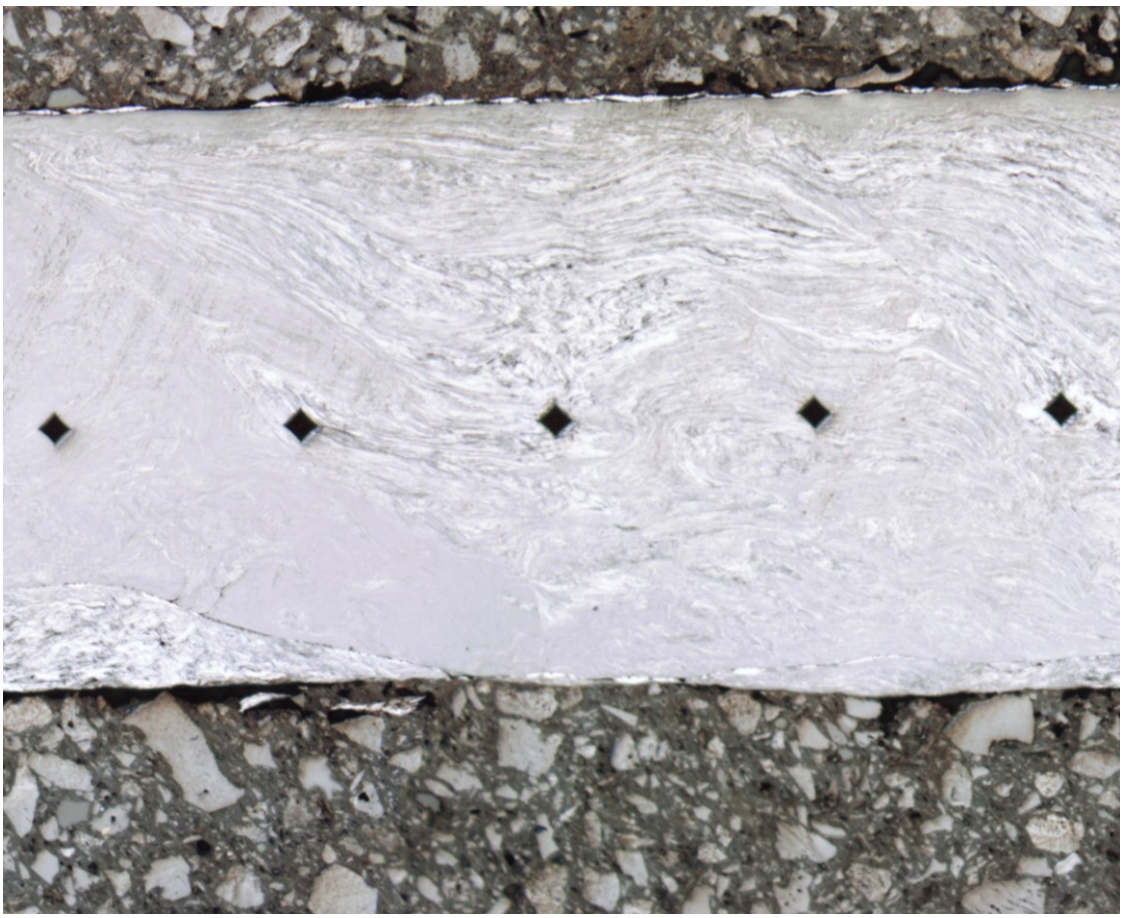

Fig. 4.9: Detailed view from R_1 = 2.5 mm to R_2 = 3.5 mm of the profile of sample #2.

“One step” HPT – Sample #2 heat treated

Fig. 4.10: Profile of the heat treated sample #2 ht, showing half of the HPT sample.

In Fig. 4.10 and Fig. 4.11 the heat treated sample #2 is examined. There is not a great difference compared to the non heat treated sample #2 in Fig. 4.8 and Fig. 4.9. The scatter of the microhardness values in the range from R = 2.5 mm to R = 3.5 mm can be explained by the deformation striations. In Fig. 4.10 this striations look like a waved pattern. Depending on the area, in which the indents were made (grey area: finer microstructure sequentially, black-white area: coarser microstructure sequentially) the hardness values show higher (→ grey area) or lower (→ black-white area) values.

Fig. 4.11: Detailed view from R_1 = 2.5 mm to R_2 = 3.5 mm of the profile of sample #2 ht.

“Two step” HPT – Sample #3

Fig. 4.12: Profile of sample #2, showing half of the HPT sample with microhardness indents.

The “two step” HPT sample showed more constant microhardness values compared to the “one step” samples. This can be confirmed by the light-optic microscopic images shown in Fig. 4.12 and Fig. 4.13. The black-white areas are brighter than in the previous pictures. The wavy pattern is not exhibited, resulting in a better homogeneity along the radial direction.

Fig. 4.13: Detailed view from R_1 = 2.5 mm to R_2 = 3.5 mm of the profile of sample #3.

“Two step” HPT – Sample #3 heat treated

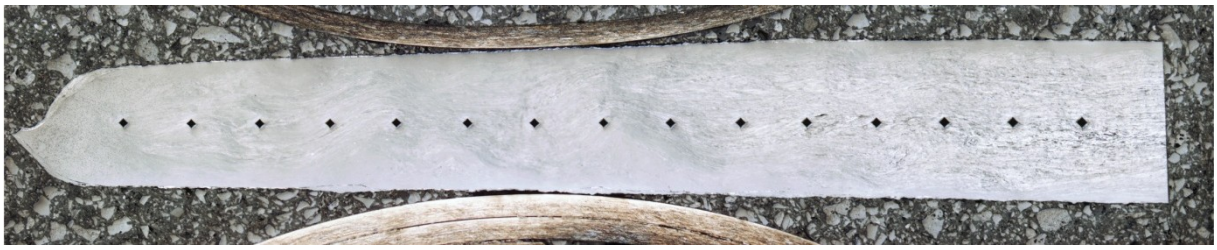

Fig. 4.14: Profile of heat treated sample #3 ht, showing half of the HPT sample with micro-hardness indents.

Fig. 4.14 and Fig. 4.15 show the heat treated sample, processed via “two step” HPT process. Except in the centre point of the sample, where still black-white areas can be seen, the sample exhibits a high homogeneity especially in the area from R_1 = 2.5 mm to R_2 = 3.5 mm.

Fig. 4.15: Detailed view from R_1 = 2.5 mm to R_2 = 3.5 mm of the profile of sample #3 ht.

In summary, the microstructural characterization by light-optic microscopy (LOM) practically confirmed the results obtained by microhardness measurements. A huge difference between the different samples was achieved. Whereas sample #1 exhibits a microstructure which could be resolved with LM techniques (→ black-white areas), the microstructure of the samples with high number of revolutions was non resolvable (→ grey areas).

The heat treated "two step" HPT sample (sample number #3-g) showed along the radial direction the highest homogeneity. What is more especially in a radius of R_1 = 2.5 mm to a radius of R_2 = 3.5 mm a very fine microstructure was received and could not be resolved by LM techniques with any magnification.

Further investigations on this sample (sample number #3 – heat treated) were carried out using scanning electron microscopy (SEM) to examine the microstructure of the composite more in detail and to estimate the grain size of the copper niobium composite.

4.2.2 Scanning electron microscopy

Characterization of the microstructure

In order to investigate the microstructure of the copper niobium composite the sample was examined by scanning electron microscopy (SEM). SEM techniques were used not only to estimate the nominal size of the composite, but also to look for an appropriate area of approximately 300 µm for the nanoindentation testing. The pictures were made in the range from R_1 = 2.8 mm to R_2 = 3.6 mm as can be seen in Fig. 4.16 on the heat treated sample number #3. As was mentioned before, this region offers the best hardness values obtained by the microhardness testing and shows the most homogeneity among the samples.

Fig. 4.16: Area for further SEM investigations on the heat treated sample #3 ht.

In Fig. 4.17 the microstructure of the composite is shown at magnification 1000 at a radius of R = 3.0 mm. Fig. 4.18 and Fig. 4.19 show the same position at higher magnifications.

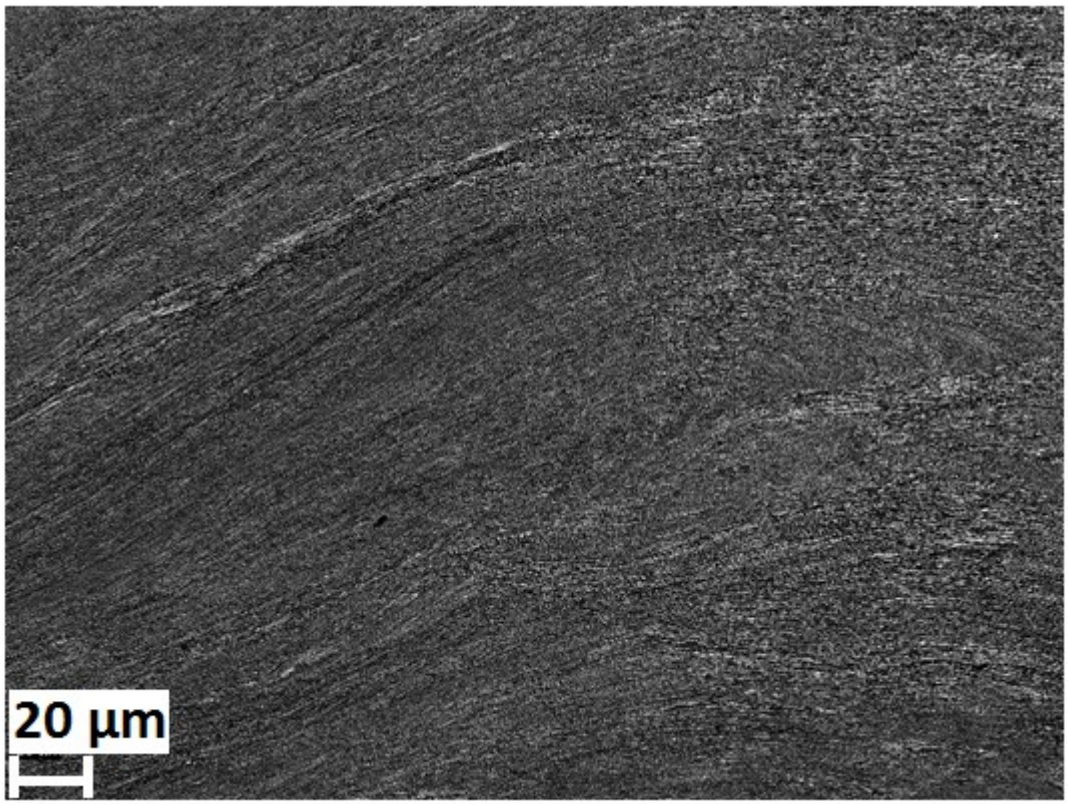

Fig. 4.17: Backscattered SEM image at R = 3.0 mm (sample #3 ht) at a magnification of 1kx.

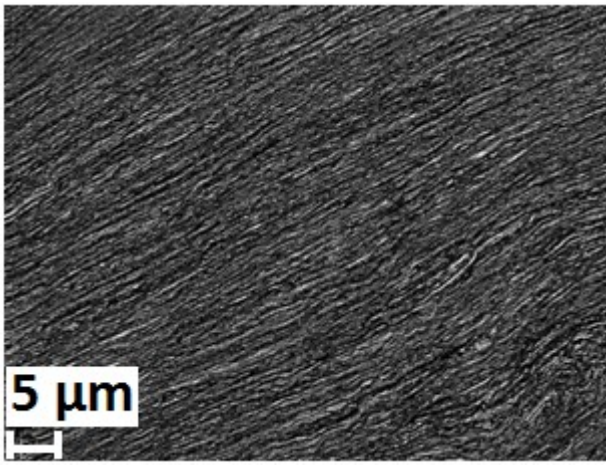

Fig. 4.18 (a): Backscattered SEM image at R = 3.0 mm at magnification 5kx.

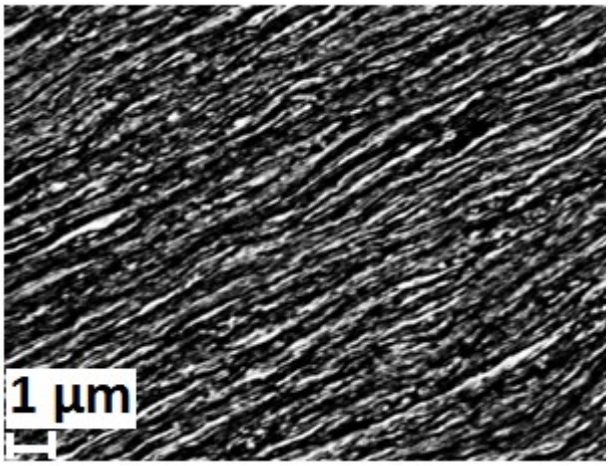

Fig. 4.18 (b): Backscattered SEM image at R = 3.0 mm at magnification 20kx.

As can be seen from Fig. 4.17 to Fig. 4.18 (a), the sample exhibited a very homogeneous and fine microstructure in the lower magnification. At higher magnifications (Fig. 4.18 (b) and Fig. 4.19) the deformation direction is apparent. From Fig. 4.19 the grain size of the composite was estimated and has a size of approximately 100 nm to 200 nm → the copper niobium is assumed to be an ultrafine grained (ufg) material.

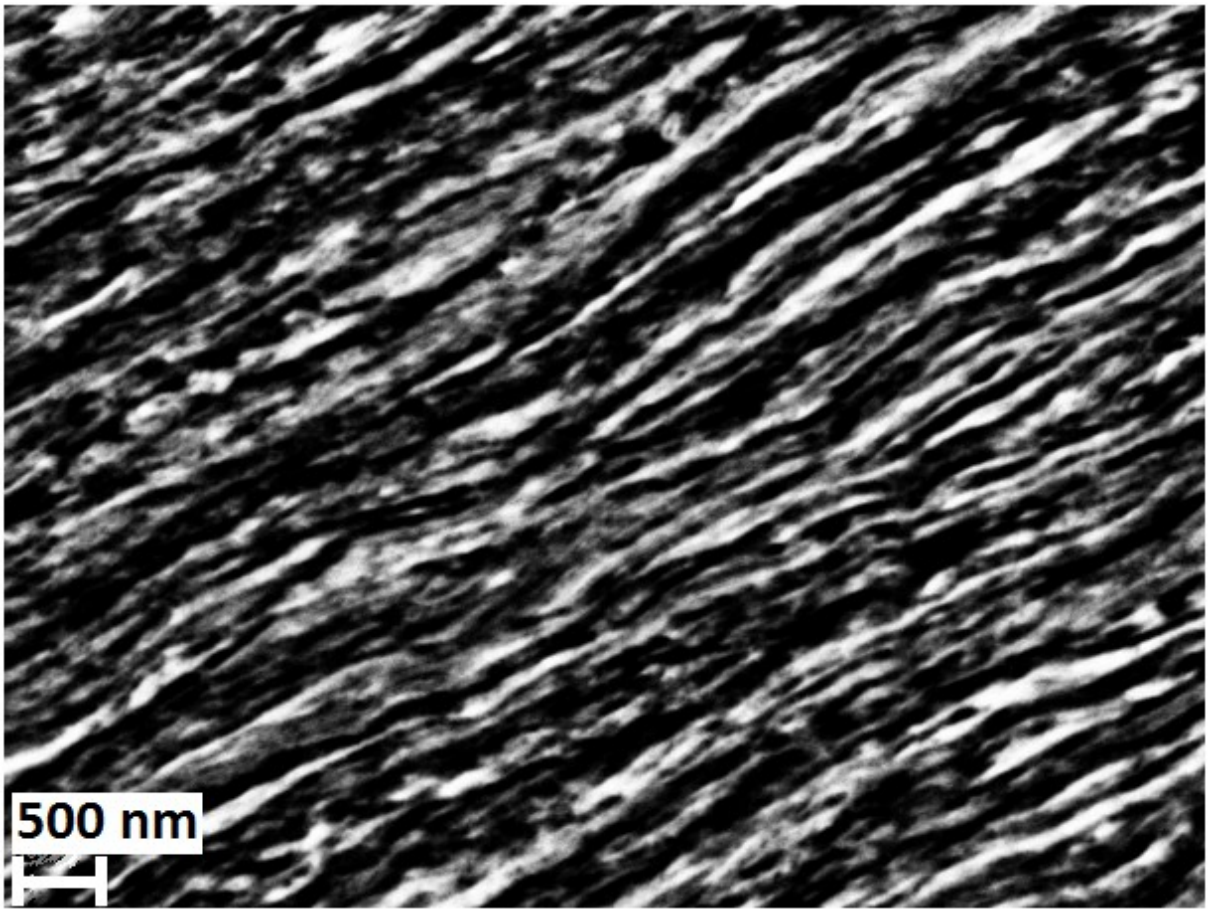

Fig. 4.19: Backscattered SEM image at R = 3.0 mm at sample #3 ht at a magnification of 40kx assuming a nominal grain size of approximately 100 to 200 nm.

Comparison of different radii at high magnification

In order to determine the optimal area for the instrumented indentation tests in agreement with the microstructural characterization by light-optic microscopy and the microhardness measurements, different radii were compared to each other. From R_1 = 2.8 mm to R_2 = 3.6 mm the microstructure was examined in 0.2 mm steps at a magnification of 20.000. Fig. 4.20 (a) to (d) show the structure of the composite at the respective radii.

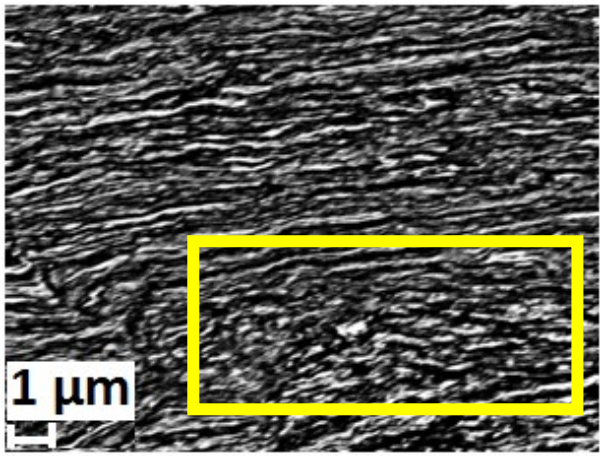

Fig. 4.20 (a): Backscattered SEM image at R = 3.6 mm of the heat treated sample #3.

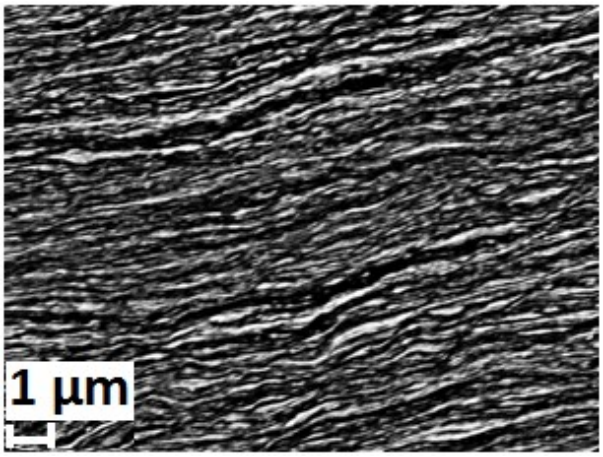

Fig. 4.20 (b): Backscattered SEM image at R = 3.4 mm of the heat treated sample #3.

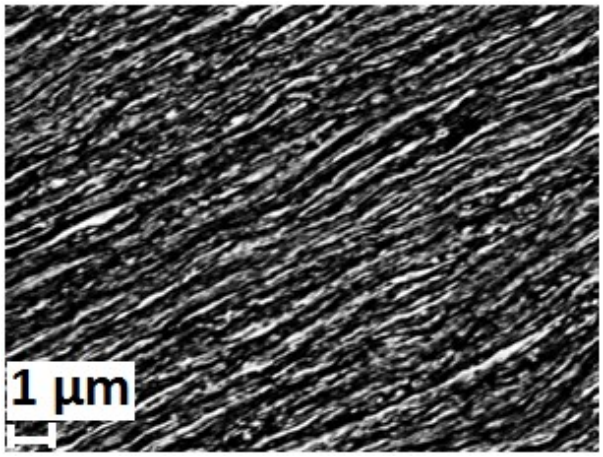

Fig. 4.20 (c): Backscattered SEM image at R = 3.0 mm of the heat treated sample #3.

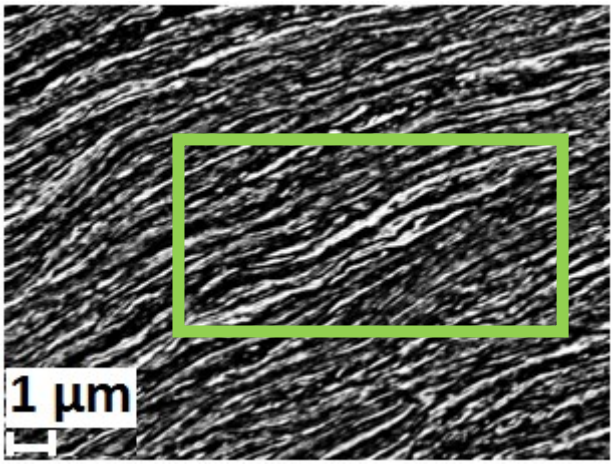

Fig. 4.20 (d): Backscattered SEM image at R = 2.8 mm of the heat treated sample #3.

At the outer region of the HPT sample at R = 3.6 mm, a saturated area is visible in the yellow rectangle in Fig. 4.20 (a). According to the microhardness measurements in a saturated area the hardness is elevated compared to non saturated regions, due to the higher plastic strains. The disadvantage of the outer region and the finer microstructure is that it is not repeatable. At R = 2.8 mm deformation striations with a thickness of approximately d = 500 nm are observed in the green rectangle in Fig. 4.20 (d). This is an indicator for lower homogeneity of the nominal structure size. Instead of the alignment of the deformation striations, Fig. 4.20 (b) and (c) show nearly the same microstructure over a field of around 400 µm.

To sum up, the nominal microstructure size of the copper niobium composite ranges approximately between 100 to 200 nm. Therefore the investigated composite has an ultra-fine grained (ufg) structure. The deformation striations are visible even if the sample was heat

treated at a high temperature of 500 °C; a transformation to globular grains was not observed (as has been reported for other copper niobium composites after annealing according to Misra et al. [5]).

Nanoindentation tests should be carried out between the two radii R = 2.6 mm and R = 3.4 mm, for example in the range from a radius of R = 2.8 mm to a radius of R = 3.2 mm. This region is offering an area of approximately 400 µm with nearly constant microhardness values and a homogeneous microstructure.

4.3 Nanoindentation hardness testing

4.3.1 Load – displacement curves

Test run at room temperature

A pre-experimental run was carried out in order to figure out the optimal testing conditions for further instrumented indentation measurements. The sample #5 was mounted with super glue on a common sample holder. The area function calibration was performed on fused silica prior to the indents. In the following figures load – displacement curves are shown.

The first experiment (Fig. 4.21 (a)) was performed to evaluate the required load for an appropriate indentation depth. A depth controlled method was used, where the minimum depth was set to 500 nm and the maximum depth to 1200 nm. Further particulars are shown in Table 4.3.

Table 4.3: Testing parameters for test run at room temperature.

Name	Unit	Value
Loading Rate	mN/s	10
Unloading Rate	mN/s	20
Dwell Period at Maximum Load	s	30

According to the received results a load of 100 mN has been chosen as advisable load for further tests. This decision was made due to the fact that the area function of the indenter showed the best results in the range from 600 to 1000 nm. A load of 100 mN results in a

maximum indentation depth of approximately 800 nm and a plastic depth of approximately 700 nm.

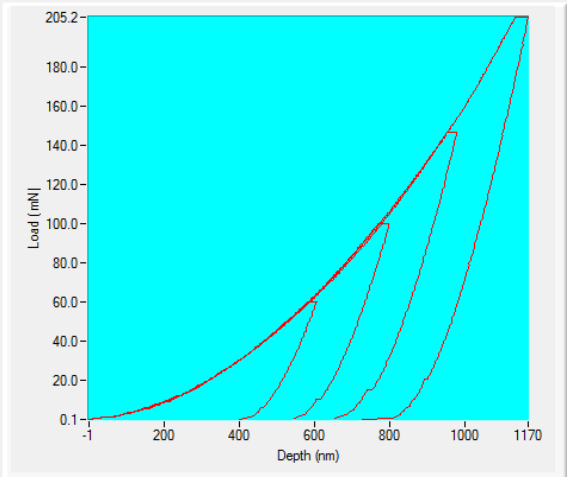

Fig. 4.21 (a): Depth controlled indents from 500 to 1200 nm maximum penetration depth.

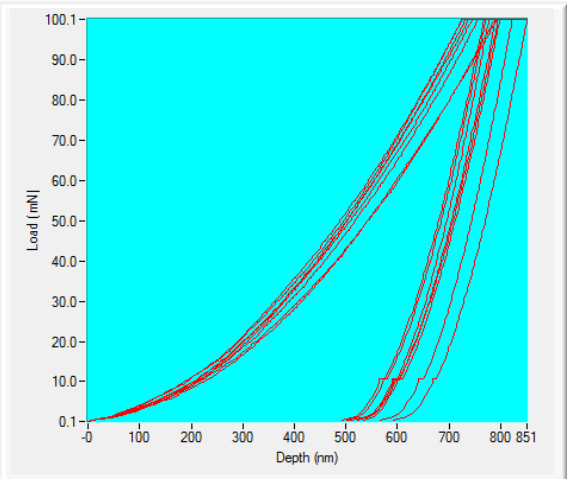

Fig. 4.21 (b): Load controlled test indents with P_{max} set to 100 mN.

Additional tests were performed (Fig. 4.21 (b)) with a load of 100 mN but different conditions (shown in Table 4.4) compared to the first experiments. The major modifications were a load controlled method and an extended dwell time in order to achieve a relaxation behaviour of the material.

Table 4.4: Testing parameters for additional nanoindentation tests.

Name	Unit	Value
Load Time	s	10
Unload Time	mN/s	5
Dwell Period at Maximum Load	s	300

The observed dwell period data is shown in Fig. 4.22 for indent #8. According to Peykov et al. [22], it is possible to measure time-dependent properties – the strain rate sensitivity (SRS) and the activation volume (V*) – with this type of experiments. This short time creep tests were already mentioned in chapter 2.2, and will be discussed in-depth later in this work.

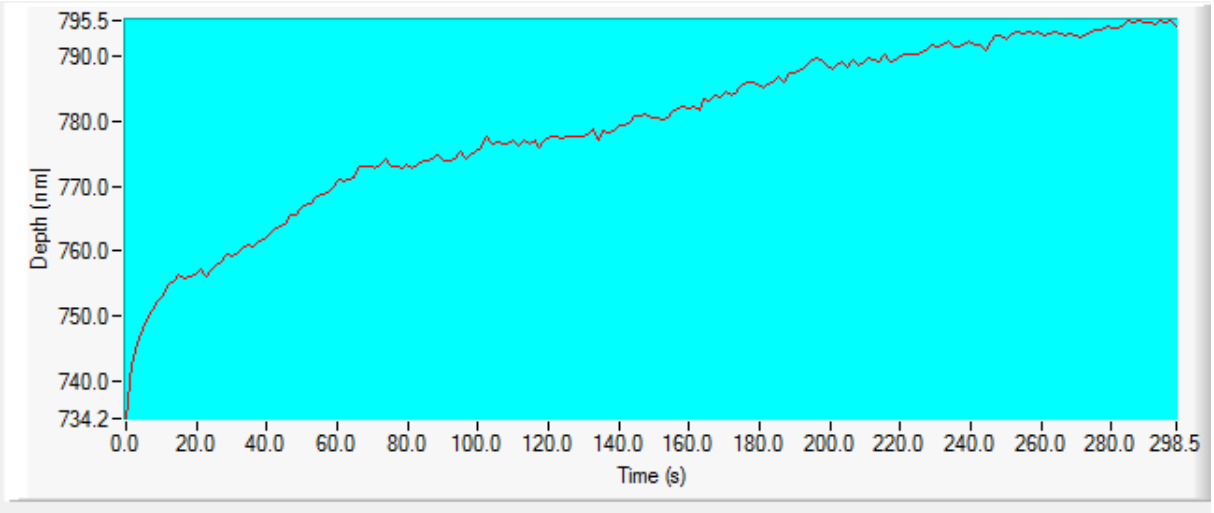

Fig. 4.22: Relaxation data at maximum load over a duration of the holding segment of 300s; room temperature measurement, Indent number 8.

A second method to determine time-dependent properties – SRS and V* – is the constant strain rate (CSR) method. The CSR method was discussed in chapter 2.2. In Fig. 4.23 (a) and Fig. 4.23 (b) the load – displacement curves of the CSR set are shown.

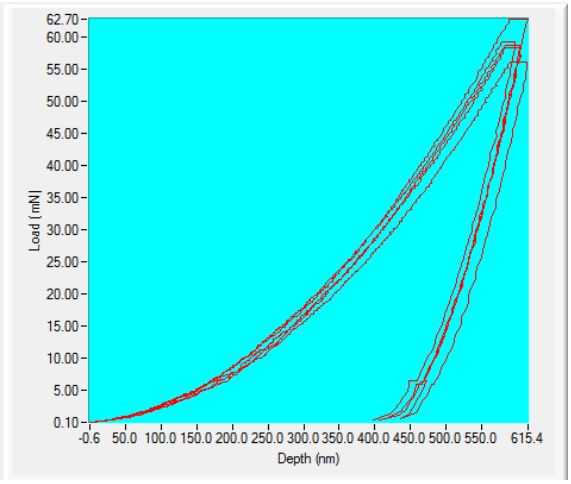

Fig. 4.23 (a): Depth controlled test indent with a proportional constant of k = 0.1.

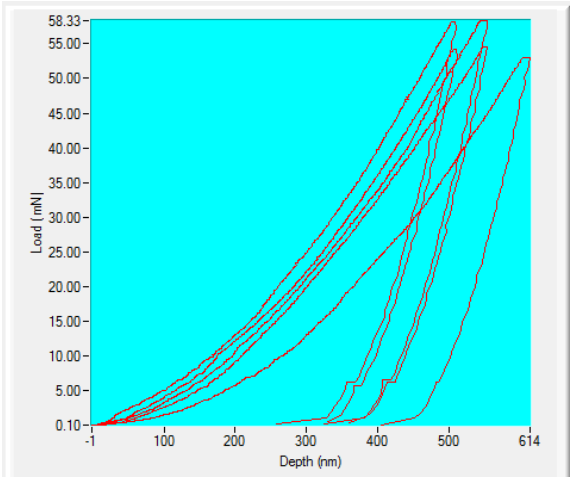

Fig. 4.23 (b): Depth controlled test indent with a proportional constant of k = 0.01.

The measurements were performed in the depth controlled method with a proportional ramp type. Further particulars can be seen in Table 4.5. The difference between these two tests was the proportional constant, which determined the strain rate.

Table 4.5: Testing parameters for depth controlled CSR measurements.

Name	Unit	Value
Unloading Rate	mN/s	20
Dwell Period at Maximum Load	s	30

Due to the apparent scatter of the load – displacement curves, especially in Fig. 4.23 (b), and hence difficult analysis of the data, the CSR method was refused.

First experimental run

The first experimental run was performed on the sample #6 from room temperature to an end temperature of 300 °C. In order to investigate basic mechanical properties, as hardness and Young's modulus, as well as time-dependent properties, as strain rate sensitivity and activation volume, five different experimental sets varying in the dwell time period (load controlled method) and in the proportional constant (depth controlled method) were carried out. In Fig. 4.24 to 4.27 the obtained load – displacement curves are shown for both load controlled settings. These curves are used to calculate the before mentioned mechanical properties as a function of temperature. The depth controlled tests were discarded, due to the fact that they exhibited high scattering and noise induced errors.

In the first experimental run the loading and the unloading rate, as well as the strain rate were kept constant for each indentation set-up. The different rates are outlined in Table 4.6.

Table 4.6: Testing conditions for the first experimental run.

Name	Unit	Value
Loading Rate	mN/s	10
Unloading Rate	mN/s	5
Strain rate at the end of loading segment	-	0.1

The load – displacement curves obtained from the room temperature measurements are shown in Fig. 4.24 (a) and (b). As can be seen in the diagrams, one of the differences between them is the longer hold segment at maximum load in Fig. 4.24 (b), caused by the longer dwell time period compared to Fig. 4.24 (a). The experimental settings are shown in Table 4.7.

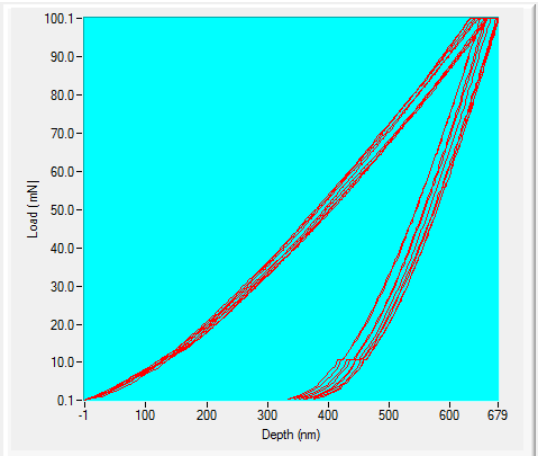

Fig. 4.24 (a): Load controlled at RT for 5 s.

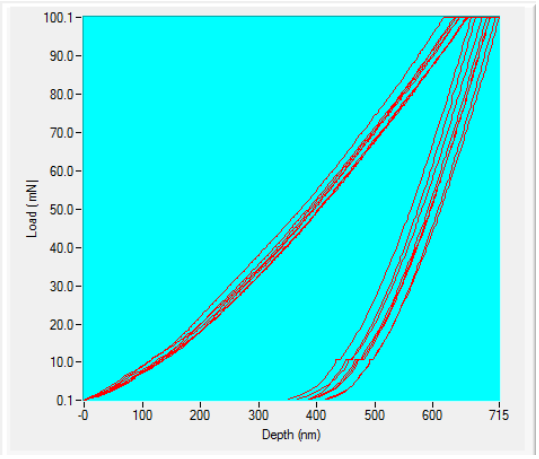

Fig. 4.24 (b): Load controlled at RT for 300 s.

Additional to the adjustments of the experimental set-up the thermal drift correction data is shown in Table 4.7. The thermal drift was calculated over final 60% of the data.

Table 4.7: Experimental conditions for the first run at room temperature.

Name	Unit	Figure 4.24 (a)	Figure 4.24 (b)
Temperature	°C	27	27
Dwell Period at Maximum Load	s	5	300
Thermal drift (60% of data)	nm/s	<0.07	<0.10

After the measurements at room temperature experiments were performed at elevated temperatures. The sample #6 on the hot stage sample holder as well as the indenter tip was subsequently heated up to a temperature of 100 °C. The heating segment was followed by a holding segment for thermal stabilization. The temperature was raised in 100 °C-steps from 100 °C to a final measurement temperature of 300 °C in the first experimental run.

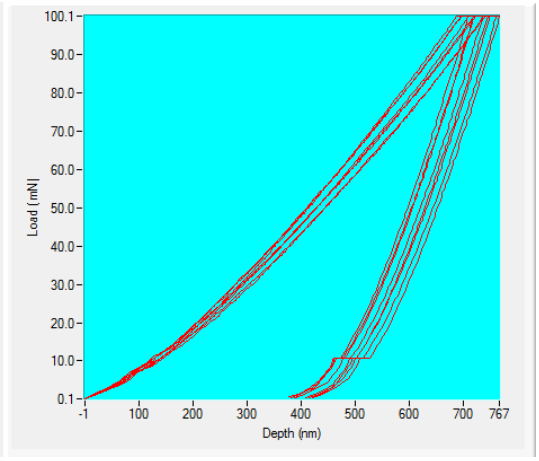

Fig. 4.25 (a): Load controlled run at 100 °C.

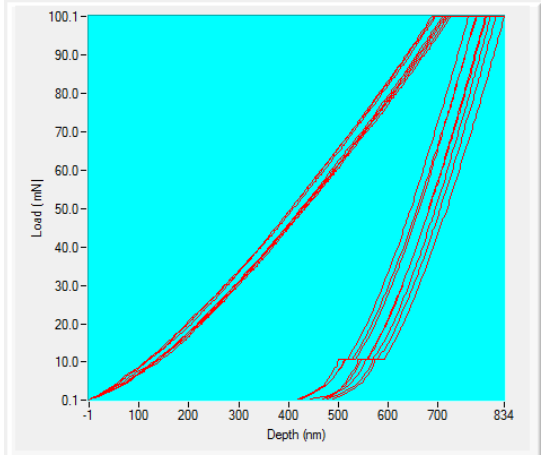

Fig. 4.25 (b): Load controlled run at 100 °C.

Fig. 4.25 (a) and (b) show the load – displacement curves obtained from indentation testing at 100 °C. Compared to the room temperature measurements, a slightly higher penetration depth is obtained and a higher thermal drift. Further particulars are shown in Table 4.8.

Table 4.8: Experimental conditions for the first run at 100 °C.

Name	Unit	Figure 4.25 (a)	Figure 4.25 (b)
Temperature	°C	100	100
Dwell Period at Maximum Load	s	5	300
Thermal drift (60% of data)	nm/s	<0.17	<0.22

After indentation measurements at 100 °C the sample and the tip were heated up to 200 °C. The load – displacement curves in Fig. 4.26 (a) and Fig. 4.26 (b) show the results at 200 °C. Compared to the previous curves, these show especially in the case of the longer holding segment a slightly higher scattering and a significant higher maximum penetration depth. The thermal drift data is shown in Table 4.9, whereas the maximum occurring thermal drift rate is under 0.30 nm drift per second.

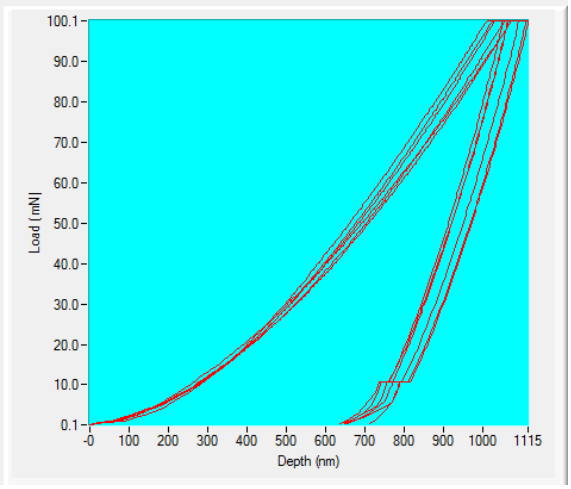

Fig. 4.26 (a): Load controlled run at 200 °C.

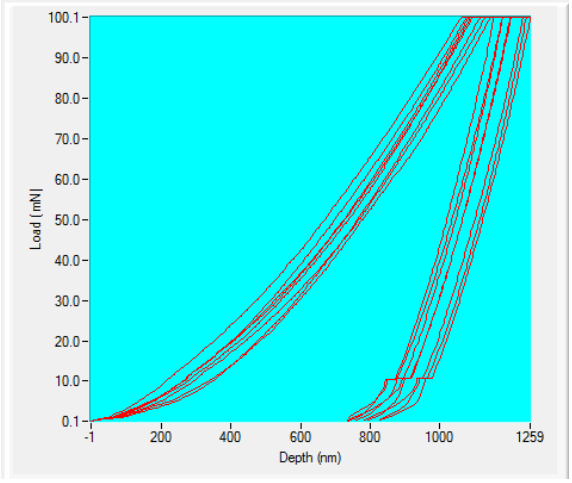

Fig. 4.26 (b): Load controlled run at 200 °C.

Table 4.9: Experimental conditions for the first run at 200 °C.

Name	Unit	Figure 4.26 (a)	Figure 4.26 (b)
Temperature	°C	200	200
Dwell Period at Maximum Load	s	5	300
Thermal drift (60% of data)	nm/s	<0.28	<0.20

The first experimental run was completed by measuring the specimen at 300 °C. The received load – displacement curves are shown in Fig. 4.27 (a) and 4.27 (b), whereas again a higher penetration depth and scattering were obtained. Table 4.10 shows the thermal drift, which is comparable to the drift of the previous measurements. The major difference to prior load – displacement data was the different shape of the individual indent curves, indicating a change in the test set-up.

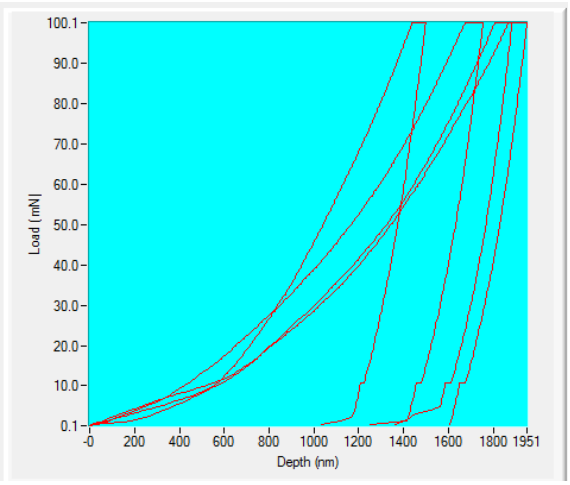

Fig. 4.27 (a): Load controlled run at 300 °C.

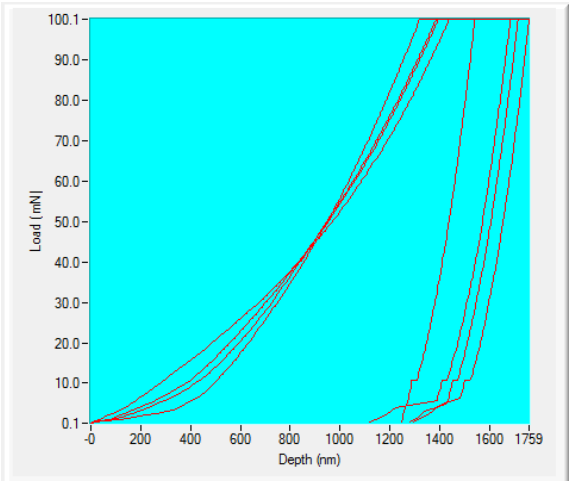

Fig. 4.27 (b): Load controlled run at 300 °C.

Table 4.10: Experimental conditions for the first run at 300 °C.

Name	Unit	Figure 4.27 (a)	Figure 4. 27 (b)
Temperature	°C	300	300
Dwell Period at Maximum Load	s	5	300
Thermal drift (60% of data)	nm/s	<0.24	<0.29

The indenter tip was examined under a light-optical microscope. A silver shiny coating could be recorded. It was assumed that the indenter tip was coated with niobium as well as the tip geometry. Thus a new area function of the tip was calculated with the fused silica calibrating sample. The area function of the cBN indenter before the high temperature measurements and after the measurements at elevated temperatures is shown in table 4.11.

Table 4.11: Area function parameters before and after the first experimental run.

Condition	Parameter a	Parameter b	Parameter c
Before heat treatment	20.09	24500.00	281088.76
After heat treatment	14.71	22683.20	157042.69

Furthermore it was assumed that the indenter tip changed at 200 °C and thus the new area function should be applied from this point when analysing the load – displacement curves. In other words: the room temperature and 100 °C data were analysed with the area function before the heat treatment; the 200 °C and 300 °C data with the second area function.

Second experimental run

The second experimental run was performed on sample #7 starting at 300 °C to a maximum temperature of 500 °C. In order to verify the data from the first experimental run, the second run started with measurements at 300 °C. In this run only two experimental settings with the load controlled method were carried out, whereas the maximum load was decreased to 30 mN. This change was necessary, in order to avoid very high maximum penetration depths. The strain rate was kept constantly to 0.1, as in the first experimental run.

The load – displacement curves obtained from the testing temperature at 300 °C are shown in Fig. 4.28 (a) and Fig. 4.28 (b). As can be seen from Table 4.12 the thermal drift was higher compared to the first run 300 °C measurements. The drift rate exceeds 0.5 nm per second, resulting in a few acceptable load – displacement curves. As in the first run the data differed from each other in the curve shape, indicating a change of the indenter tip geometry.

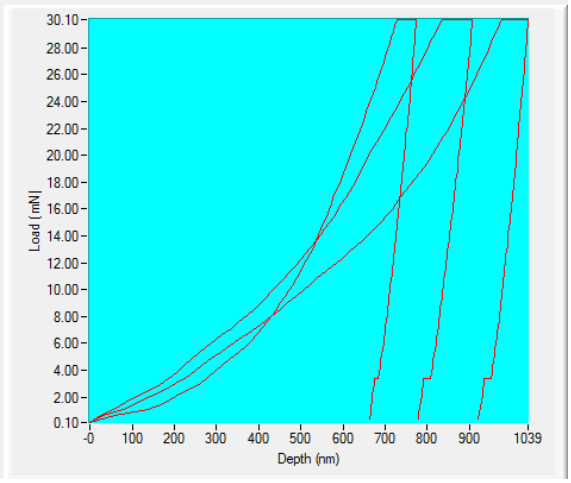

Fig. 4.28 (a): Load controlled run at 300 °C.

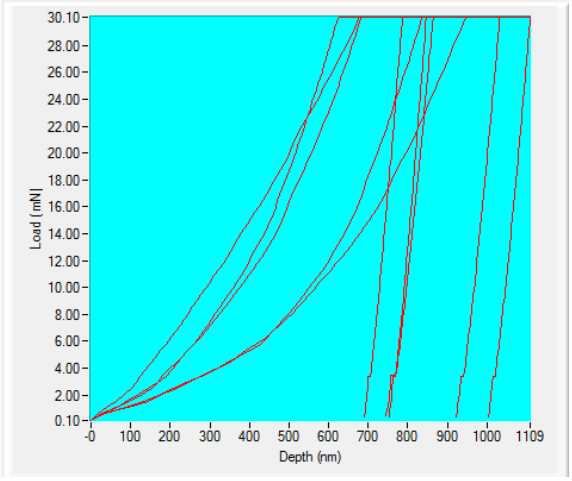

Fig. 4.28 (b): Load controlled run at 300 °C.

Table 4.12: Experimental conditions for the second run at 300 °C.

Name	Unit	Figure 4.28 (a)	Figure 4.28 (b)
Temperature	°C	300	300
Dwell Period at Maximum Load	s	5	300
Thermal drift (60% of data)	nm/s	<0.53	<0.30

The sample was heated up after the indentations to 400 °C. For the most part the load – displacement curves at this testing temperature exhibited strange curves. Thus only two curves for the short and the long dwell period were appropriate for further investigations.

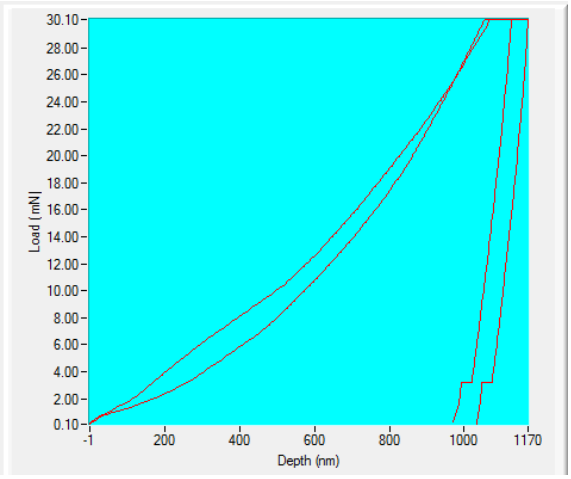

Fig. 4.29 (a): Load controlled run at 400 °C.

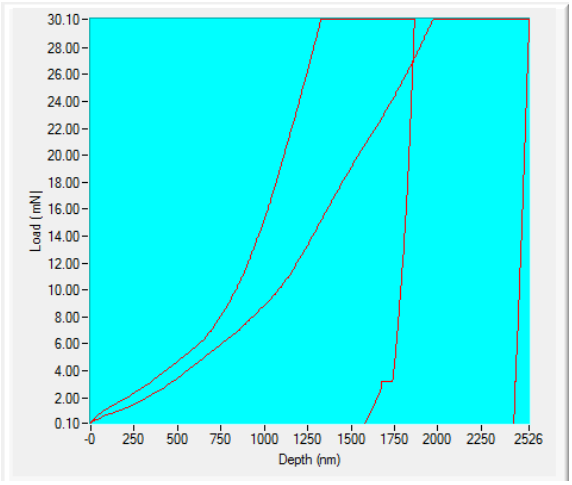

Fig. 4.29 (b): Load controlled run at 400 °C.

In Table 4.13 the maximum thermal drift rate of the 400 °C measurements are shown. The details showed similar values as for the previous 300 °C tests. Due to this fact the uncommon curves could not be explained by drift induced errors. It was assumed that an explanation for this circumstance could be

Table 4.13: Experimental conditions for the second run at 400 °C.

Name	Unit	Figure 4.29 (a)	Figure 4. 29 (b)
Temperature	°C	400	400
Dwell Period at Maximum Load	s	5	300
Thermal drift (60% of data)	nm/s	<0.48	<0.30

The results from Fig. 4.30 (a) and Fig. 4.30 (b) of the 500 °C measurements exhibited high penetration depths especially in the relaxation testing with the long holding segment at maximum load (Fig. 4.30 (b)). What is more, as shown in Table 4.14, the thermal drift exceeded by far a thermal drift of 1.0 nm per second. Due to this fact the analyzing and data processing of the 500 °C data should be handled with care.

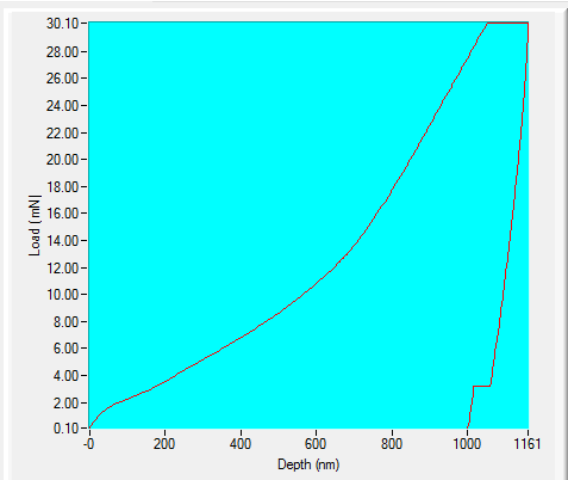

Fig. 4.30 (a): Load controlled run at 500 °C.

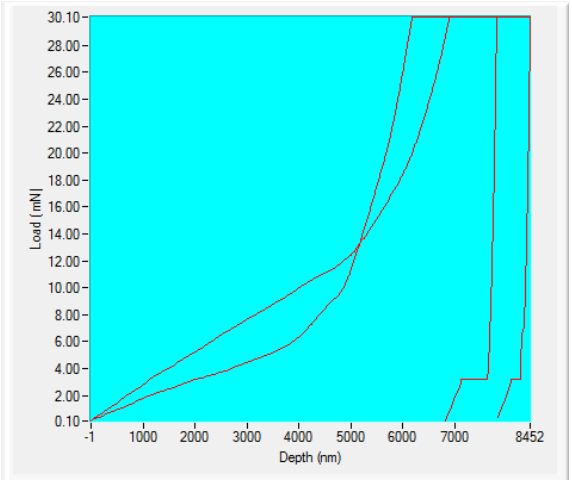

Fig. 4.30 (b): Load controlled run at 500 °C.

Table 4.14: Experimental conditions for the second run at 500 °C.

Name	Unit	Figure 4.30 (a)	Figure 4.30 (b)
Temperature	°C	500	500
Dwell Period at Maximum Load	s	5	300
Thermal drift (60% of data)	nm/s	<1.19	<1.60

Subsequently after the measurements at higher temperatures a new calibration of the indenter tip area function was carried out in order to verify the shape and the geometry of the cBN indenter. The same assumption was made as in the first experimental run (modification of the indenter tip during a high temperature testing). Because of this assumption the load – displacement curves were analysed with the area function after the heat treatment. In Table 4.15 the area function is shown prior and after the heating. It has to be noted, that the frame compliance has been changed, from 0.305 to 0.45, in order to obtain a proper fitting for the fused silica values.

Table 4.15: Area function parameters before and after the second experimental run

Condition	Parameter a	Parameter b	Parameter c
Before heat treatment	23.66	7470.55	-40290.39
After heat treatment	15.57	13981.31	----------

4.3.2 Hardness as a function of temperature

The hardness of the copper niobium composite as a function of temperature obtained from the nanoindentation experiments is shown in Fig. 4.30. In order to assess the hardness values the load – displacement curves with the short dwell time at maximum load (5 seconds) were used to avoid any kind of relaxation of the material. The hardness values were calculated by equation 2.1 from chapter 2.2 – dividing the maximum load (P_{max}) by the contact area (A_c).

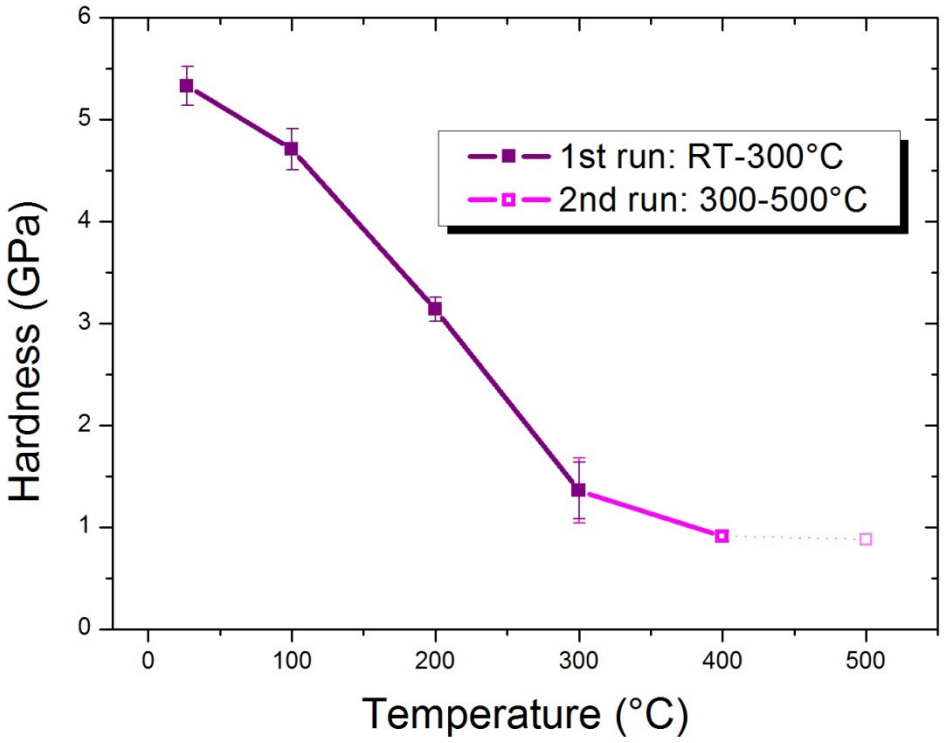

Fig. 4.30: Hardness as a function of temperature obtained from the first experimental run (purple curve) and the second experimental run (pink curve).

The purple curve shows the results from the first experimental run from room temperature (RT) to 300 °C, the magenta curve represents the outcomes of the measurements from 300 °C to 500 °C. The hardness values from the first run at 300 °C are in accordance with those from the second run at 300 °C. Due to the fact that only one load – displacement curve was used to calculate the hardness at the highest testing temperature, the hardness value at 500°C is illustrated pale.

At room temperature the hardness of the copper niobium composite is approximately 5.4 GPa. The composite exhibits a higher hardness compared to other nano-crystalline and

ultrafine grained material, as can be seen in Fig. 4.31. The materials shown in this figure are processed via different routes (e.g. nano-layered structures or cold-drawn wires) and in the range from 10 nm to 300 nm. Furthermore, not only different types of copper niobium composites are collated, also pure copper (orange) as well as pure niobium (silver) with different grain sizes. The copper niobium composite investigated in this work possesses the highest hardness of all materials in the ufg range – at approximately 200 nm.

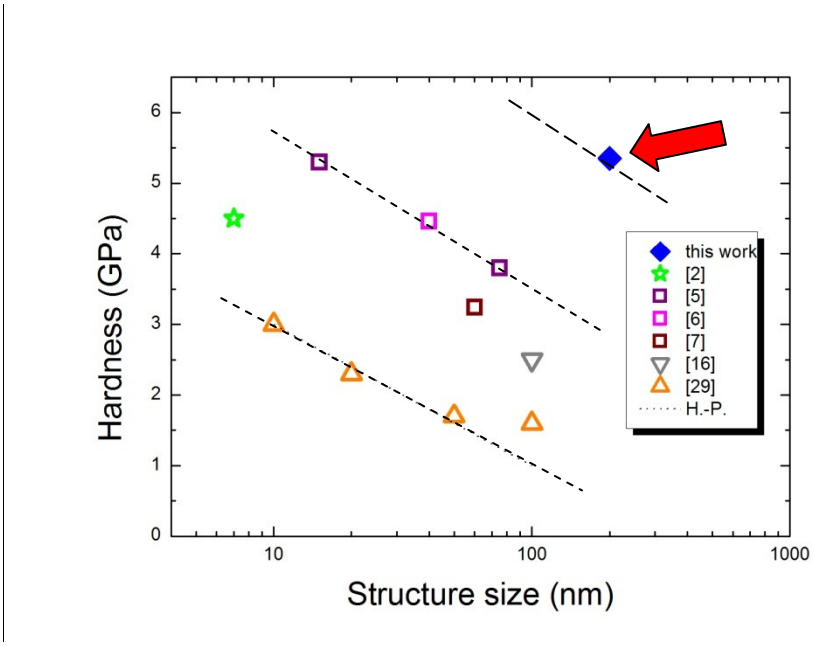

Fig. 4.31: Comparison of room temperature hardness values from different previous works.

In order to understand more about the thermal behaviour of the novel composite the received data was compared to other materials. In Fig. 4.32 the hardness as a function of temperature is shown for three different copper materials and the copper niobium composite investigated in this work. Hardness values as a function of temperature of pure niobium have not been found in the literature.

The hardness at room temperature of the copper niobium composite is higher than for nc (brown curve) [24], ufg (red curve) [25] and cg (orange curve) [26] copper. The highest hardness values are obtained for nano-crystalline copper [24]. At approximately 200 °C a decrease in the hardness values is apparent. This is caused by a grain growth of the fine grains (ufg and nc) during heat treatments. The hardness of ufg and cg copper is above 300 °C nearly the same. The investigated copper niobium composite exhibits a similar trend in the decrease. At approximately 200 °C a significant decrease in the hardness values was observed. In this range grain growth of the fine composite microstructure could occur.

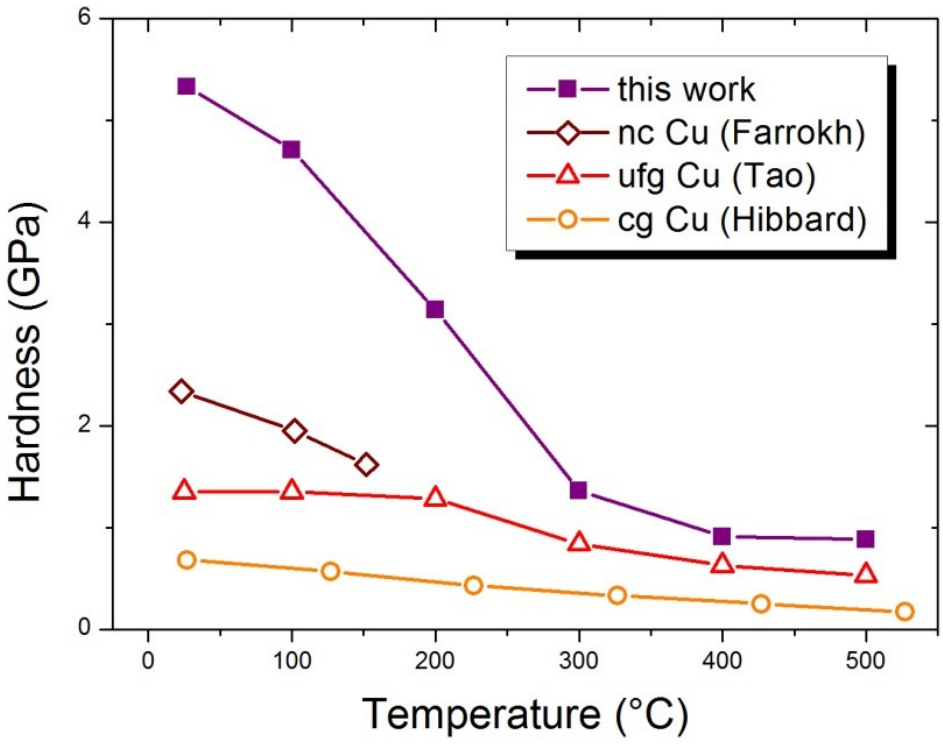

Fig. 4.32: Hardness as a function of temperature for different Cu materials compared to the copper niobium composite from this work.

In Fig. 4.33 the hardness over temperature of two different copper niobium composites are shown together with the composite investigated in this work. The curves show a significantly higher thermal stability for cold-drawn wires (nominal microstructure size of 100 nm) [4] and the copper niobium multilayer (nominal layer size of 75 nm) [5].

It has to be kept in mind, that the high thermal stability of the two composites was determined ex-situ, while hardness measurements were performed in-situ in this work. The wires were heat treated for 60 minutes under an argon atmosphere [4] and in the case of the nano-layers an annealing for 30 minutes was carried out [5]. Compared to the HPT composite in this work the other two were exposed for a much shorter time at the certain temperature (compare the temperature profile of the two experimental set-ups in chapter 3.6.2).

Furthermore the three composites differ from each other in a significant way. The copper niobium wires from [2, 3, 4] use the refractory metal niobium as an obstacle for the fine copper grains. The grain boundaries are pinned by these obstacles during a heat treatment, resulting in a fine microstructure even at high temperatures. The fine dispersed Nb – in the range of several nm – does not conglomerate because of the high melting point.

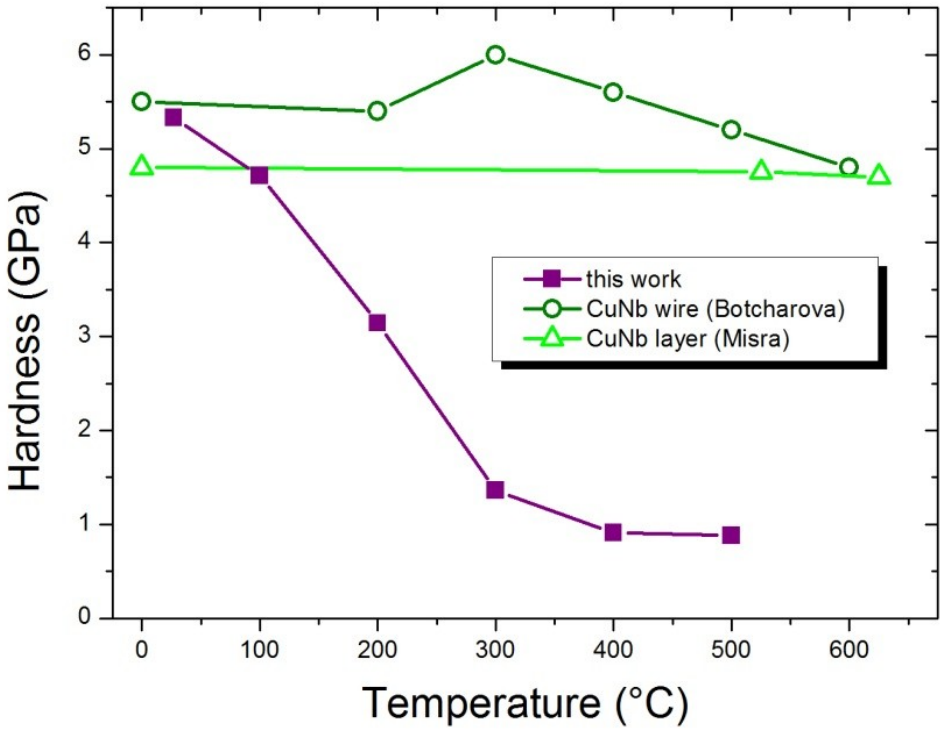

Fig. 4.33: Thermal stability for CuNb wires and CuNb layers compared to the composite.

4.3.3 Young's modulus as a function of temperature

The reduced modulus of the copper niobium composite as a function of temperature is shown in Fig. 4.34. The reduced modulus was calculated by equation 2.4.

The load – displacement curves with the short dwell time were used for the calculation. The measurements from the first run (purple curve) show a huge decrease in the modulus from approximately 108 GPa at room temperature to approximately 48 GPa at 300 °C.

The results obtained from the second experimental run (pink curve) exhibit a decrease too, but not as high as in the first run. Furthermore, the results from the first experimental run at 300 °C are not in accordance with the outcomes from the second experimental run at 300 °C, as it was observed in the hardness measurements.

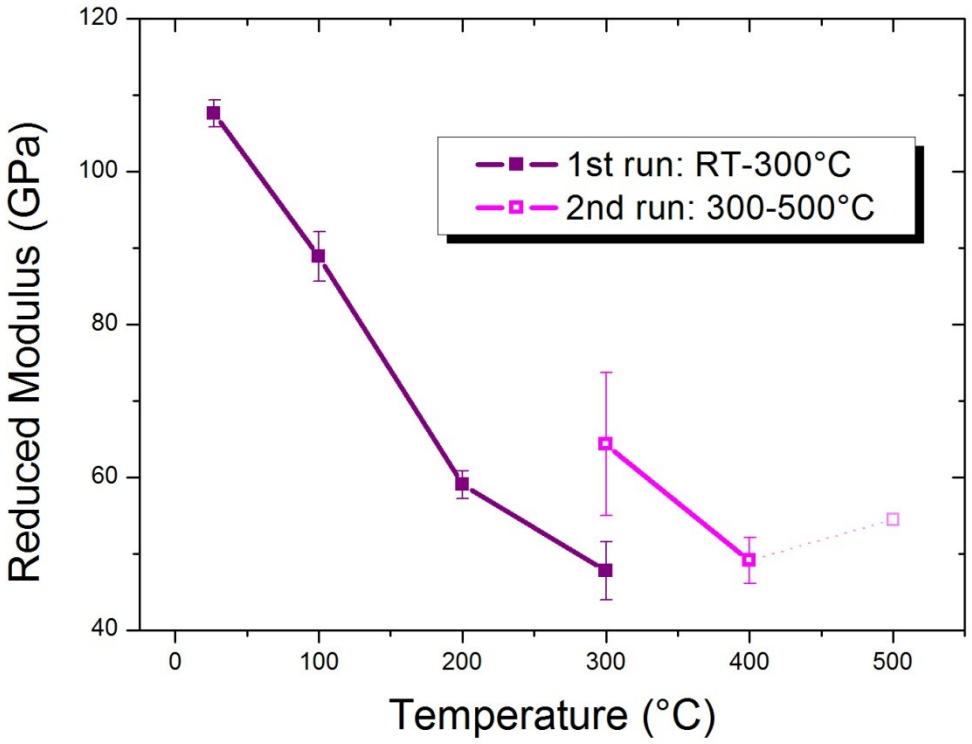

Fig. 4.34: Reduced modulus as a function of temperature obtained from the first and the second experimental run.

In order to obtain Young's modulus values out of the reduced modulus data, equation 2.5 from chapter 2.2 was used and transformed to the elastic modulus of the sample (E_s). In Table 4.16 the data for the calculation is shown, whereas the Poisson's ratio of the sample (ν_s) was calculated by a rule of mixture with the volume fraction of the composite. The data for the Poisson's ratio for copper and niobium were taken from [27].

The indenter material was cubic boron nitride. The reduced modulus as a function of temperature (E_r) was taken from the experiments. In Fig. 4.35 the Young's modulus as a function of temperature can be seen together with the reduced modulus data from Fig. 4.34.

Table 4.16: Data for the calculation of the Young's modulus with a cBN indenter.

Name	Value	Unit
Young's modulus of the indenter (E_i)	800	GPa
Poisson's ratio of the indenter (ν_i)	0.12	-
Poisson's ratio of the sample (ν_s)	0.37	-

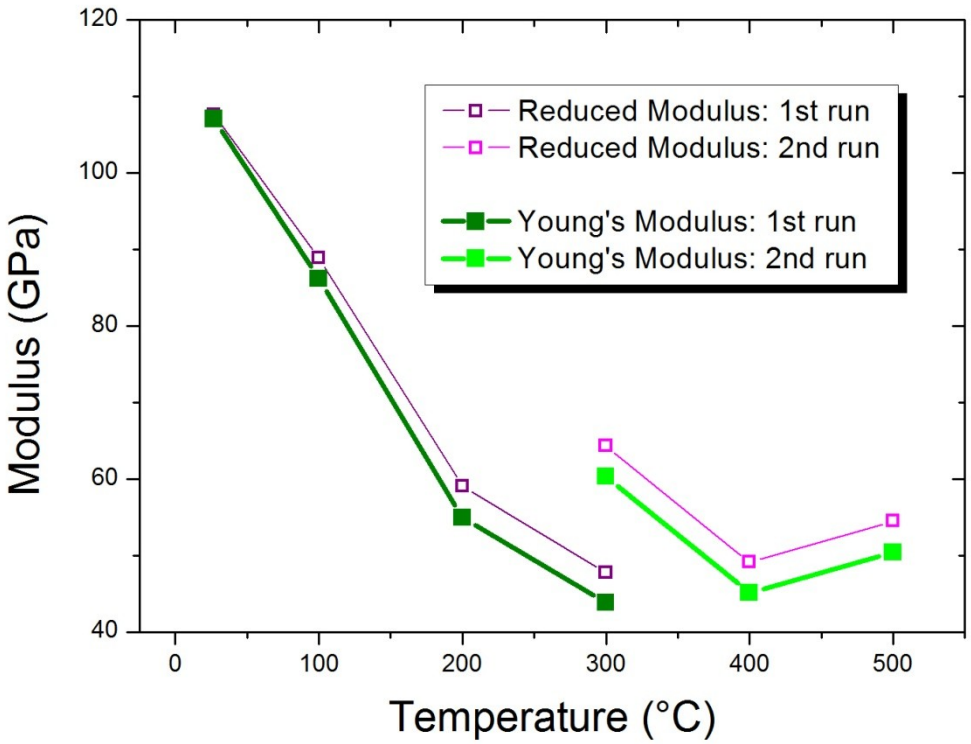

Fig. 4.35: Reduced modulus (purple) compared to calculated Young's modulus (green).

The purple and magenta curves in Fig. 4.35 indicate the reduced modulus of the composite, obtained from the indentation experiments. The dark green and light green curves show the calculated Young's modulus. The difference between these two data sets is not significant, when calculating with the Poisson's ratio and the Young's modulus of boron nitride.

In the literature the Young's modulus of a copper niobium composite has not been discussed yet. In order to compare and explain the results, a composite Young's modulus has been calculated with data from copper and niobium moduli.

In Fig. 4.36 Young's moduli of copper, niobium and a copper niobium composite as a function of temperature are shown. The data for copper (orange colour) and niobium (silver colour) are taken from [28]. The fcc material copper has a higher modulus at room temperature compared to the bcc material niobium. A significantly decrease over temperature is apparent in the case of copper, whereas the changing of the Young's modulus of niobium is negligible. The composite data was calculated by a rule of mixture using the volume fraction of the elements and the data from [28].

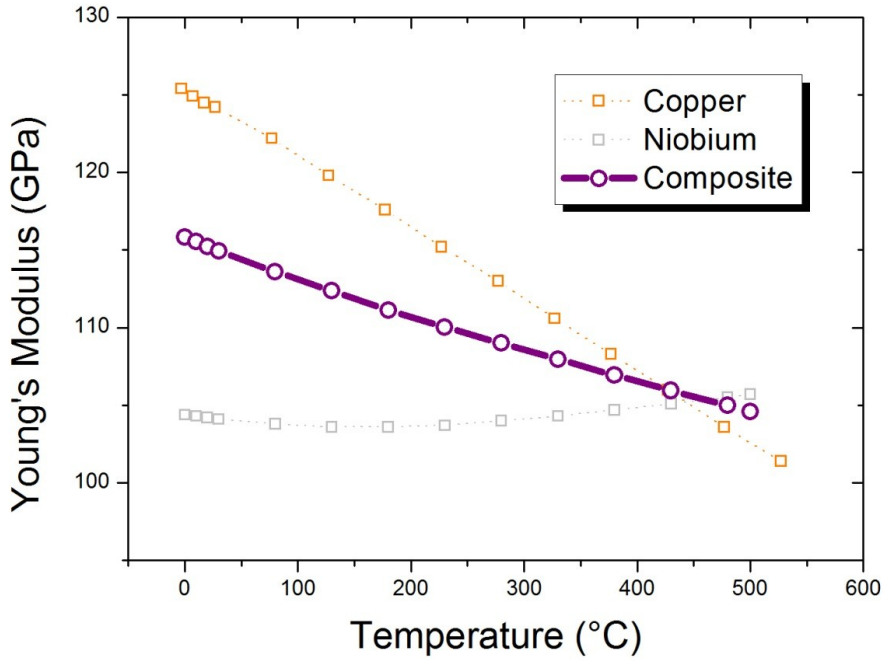

Fig. 4.36: Calculated Young's modulus of the composite from data according to [28].

According to this calculation the Young's modulus of the composite should be higher, especially at elevated temperatures, as was obtained from the nanoindentation experiments in the first and the second experimental run as can be seen in Fig. 4.37.

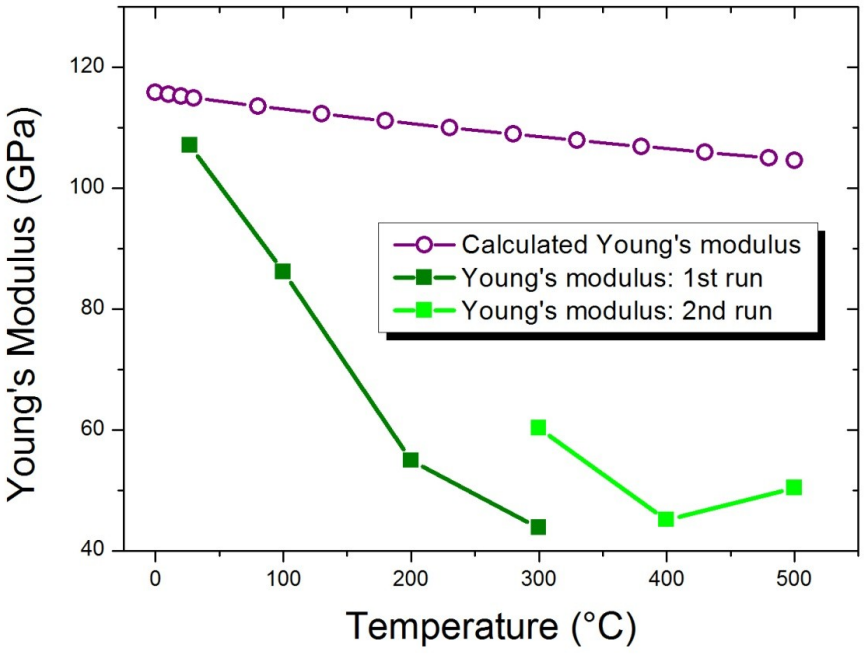

Fig. 4.37: Comparison of calculated Young's modulus and measured Young's modulus.

A possible explanation for this phenomenon is that the indenter material has changed and hence falsified frame compliance is achieved. After the indentation testing at elevated temperature the indenter tip was covered with a silver shining film. It was assumed that the indenter tip was contaminated with niobium, due to the fact that copper shines in a yellow ochre colour. Furthermore it was assumed that the contamination occurs above 100 °C.

To compensate these circumstances the indenter tip was changed to niobium instead of cubic boron nitride for the analysis. Equation 2.5 was used to calculate the Young's modulus with a different indenter tip material. In Table 4.17 the data for the calculation is shown and was taken from [27].

Table 4.17: Data for the calculation of the Young's modulus with a Nb indenter.

Name	Value	Unit
Young's modulus of the indenter (E_i)	105	GPa
Poisson's ratio of the indenter (ν_i)	0.40	-
Poisson's ratio of the sample (ν_s)	0.37	-

The corrected Young's modulus (dark cyan and cyan colour) as well as the original Young's modulus (dark green and light green colour) data can be seen in Fig. 4.38. The new corrected modulus results are approximately two times higher than the original data and exhibit a more constant trend.

In Fig. 4.39 the original Young's modulus values from the first experimental run, which were analysed with the cBN indenter, at room temperature and 100 °C are shown (dark green). Furthermore the new calculated values with the Nb indenter at 200 °C and 300 °C from the first run (dark cyan), and the values from the second run at 300 °C, 400 °C, and 500 °C (cyan) can be seen. A linear fit function was applied in order to obtain smoothed curve.

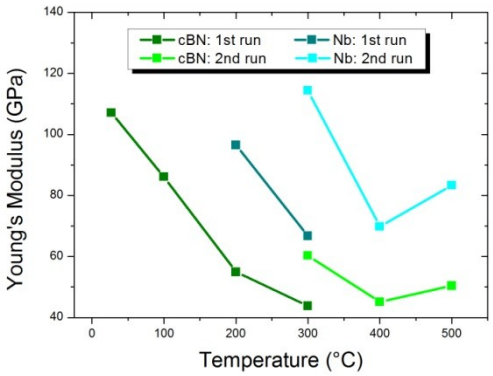

Fig. 4.38: Indenter material: cBN – Nb.

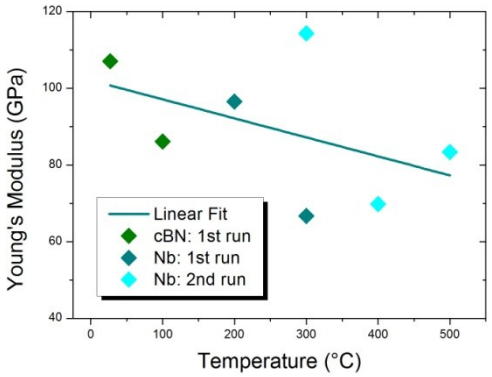

Fig. 4.39: Fitting of new Young's modulus values.

The new calculated Young's modulus data (Fig. 4.40) and the original data obtained from the instrumented indentation (Fig. 4.37) are compared to the calculated Young's modulus values of the copper niobium composite (purple curve). As can be seen in Fig. 4.40 the trend of the values is nearly the same, although the values deviate more than twenty per cent from the calculated copper niobium composite (purple curve). What is more, a sudden decrease at around 200 °C is not observed.

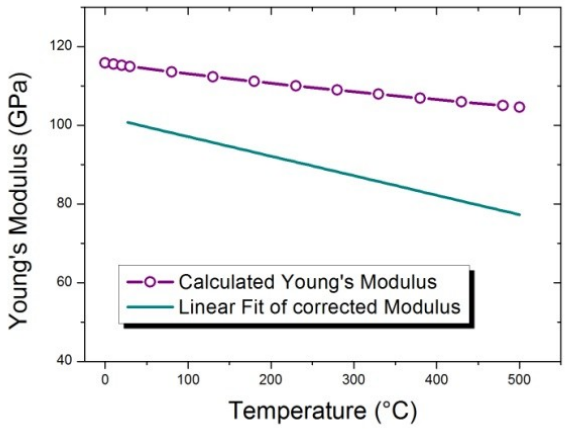

Fig. 4.40: Linear fit of corrected Young's modulus compared to calculated modulus

4.3.4 Strain rate sensitivity

Analyzing methods

The strain rate sensitivity – the SRS value – was determined by the constant load (CL) method according to [22]. The calculation was carried out in a Microsoft Office Excel sheet, while the fitting was realised in OriginPro 8. A description of the method and the equations used were discussed in chapter 2.2 of this work.

The two most important parameters for calculating the strain rate sensitivity are the natural logarithmic of the hardness over time and the natural logarithmic of the strain rate as a function of time.

In the following the procedure will be described in detail step by step with the first indent of the room temperature measurements as representative sample. For the analysis of the strain rate sensitivity the dwell period curves of the load – displacement curves with the long dwell time at maximum load (300 seconds) were used. In Fig. 4.41 the dwell curve is shown.

In order to calculate the strain rate – $\dot{\varepsilon}$ – from the displacement – h – data, the first derivative has to be generated. Due to the fact that it is almost impossible to derivate the curve in Fig. 4.41, the data has been fitted with the power law function in equation 4.2.

$$y = A * |x - x_c|^P \qquad \text{(Eq. 4.2)}$$

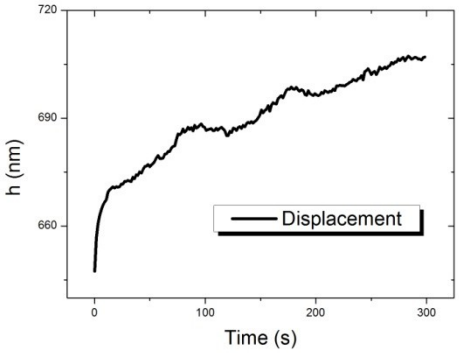

Fig. 4.41: Short time creep curve.

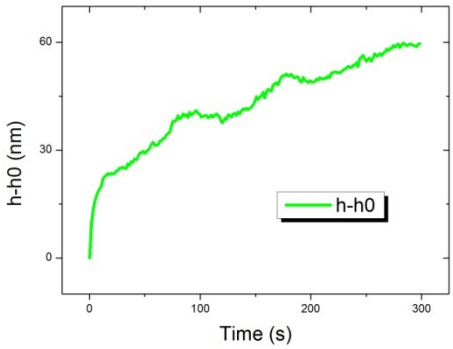

Fig. 4.42: Standardised relaxation curve.

The first step was to subtract the displacement at the beginning of the holding segment – h_0 – from all data points in Fig 4.41. The resultant curve (Fig. 4.42) is similar to the curve obtained from the measurements (Fig. 4.41), but the displacement h on the ordinate is replaced by the standardised displacement h-h_0. In order to be able to fit the displacement curve with the power law fit function from [22] this step was necessary.

In a second step, the curve exhibited in Fig. 4.42 was fitted with the above mentioned power law fit function. The received fit function (red curve) as well as the standardised displacement (green curve) data is shown in Fig. 4.43. Three parameters (x_c, A and P) were obtained from the Origin software as fitting parameters.

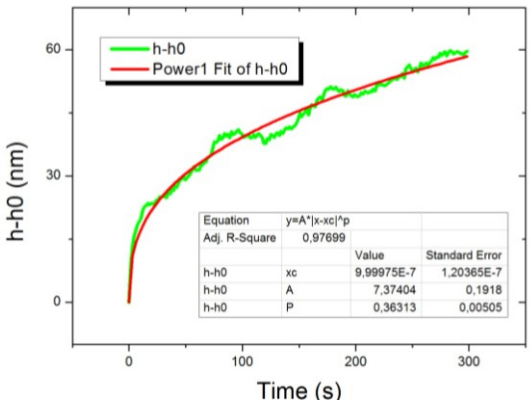

Fig. 4.43: Power law fit (red curve) of standardised relaxation curve (green).

According to Peykov [22] the (standardised) displacement curve can be divided into two stages. These two stages were named “stage a” and “stage b”, whereas “stage a” ranges from the beginning of the holding segment to 20 seconds. The so called “stage b” ranges from approximately half of the duration time of 150 seconds to the end of the holding segment. (Explanatory notes: this short time creep tests described in this work should not be mixed up with creep tests. For this reason the two stages were not specified as “stage I” and “stage II”, as it is in creep tests and were reported in [23].)

Furthermore Peykov described that the results obtained from “stage a” are in better agreement with strain rate sensitivity results from different analyzing methods than results received from “stage b”. The “stage b” results show approximately ten times higher values. Despite this fact the strain rate sensitivity of both stages, “stage a” as well as of “stage b”, was determined with the CL method; but with more attention to “stage a”.

In Fig. 4.44, a detailed view of Fig. 4.43, where only the first twenty seconds were represented, a significant discrepancy between the power law fit function (red curve) and the standardised displacement curve (green) is evident, resulting in an error in the calculation of the m-value. Because of this deviation, “stage a” and “stage b” were separately fitted with the power law fit function; for “stage a” from 0 to 20 seconds of the standardised displacement curve (Fig. 4.45), and for “stage b” from 150 to 300 seconds (Fig. 4.46).

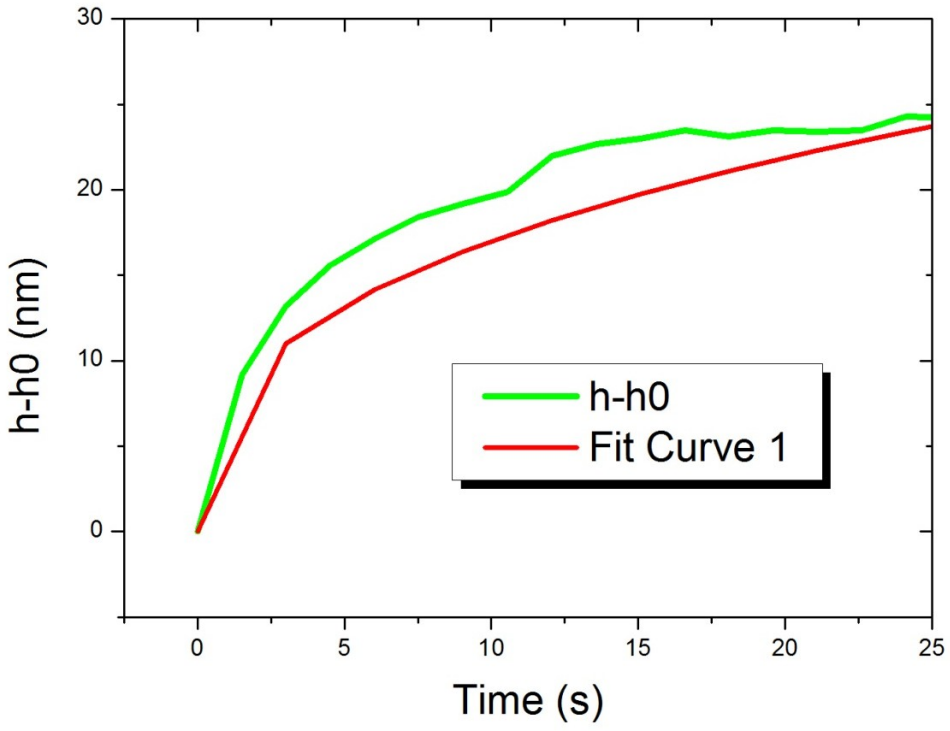

Fig. 4.44: Deviation between standardised relaxation curve (green) and fit function (red curve) in the first 20 seconds of the experiment.

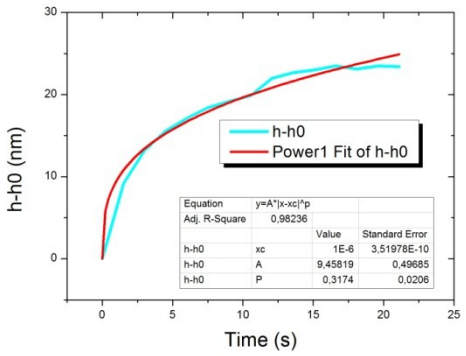

Fig. 4.45: Power law fit of "stage a".

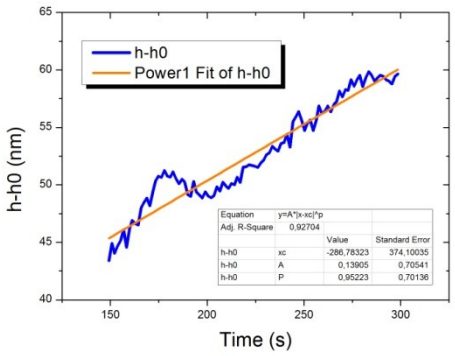

Fig. 4.46: Power law fit of "stage b".

The following steps will be described only for "stage a" due to the similarity of the analysis. After fitting the standardised displacement curve with the fit function (Fig. 4.45) the displacement at the beginning of the holding segment – h_0 – was added again to all of the data points, as can be seen in Fig. 4.47. This step has an enormous importance due to the fact that the strain rate is calculated by dividing the first derivative of the displacement by the displacement itself (h) and not by the standardised displacement (h-h_0). In Fig. 4.48 the displacement (light blue curve) and the first derivative of the displacement (dark blue curve) are shown. With these two curves it is possible to calculate the strain rate as a function of time – $\dot{\varepsilon}(T)$ – and hence the natural logarithmic strain rate as a function of time – [ln($\dot{\varepsilon}$)](T).

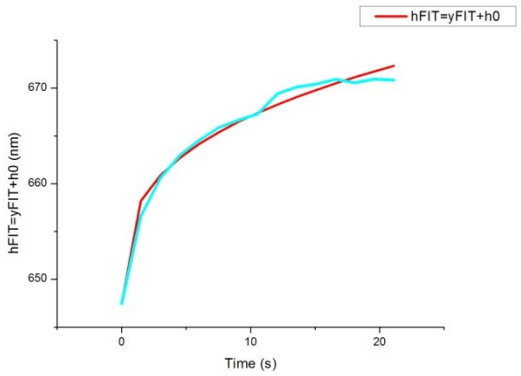

Fig. 4.47: Fitted relaxation curve in the first 20 seconds of the experiment.

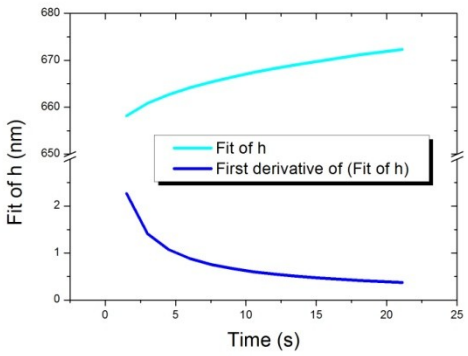

Fig. 4.48: Comparison of the displacement rate (blue) and the displacement (cyan).

The hardness as a function of time – $H(T)$ – and thus the natural logarithmic hardness over time – [ln(H)](T) – were calculated by dividing the maximal load – P_{max} – by the contact area – A_c at a specific testing time. The strain rate sensitivity is the slope of the curve in a diagram, where on the ordinate the natural logarithmic hardness as a function of time is plotted

and on the abscissa the natural logarithmic strain rate over time. This representative indent has for “stage a” a slope (light grey linear fit) and hence a strain rate sensitivity of 0.020. For “stage b” the slope (dark grey linear fit) and thus the m-value is 0.073 (Fig. 4.49).

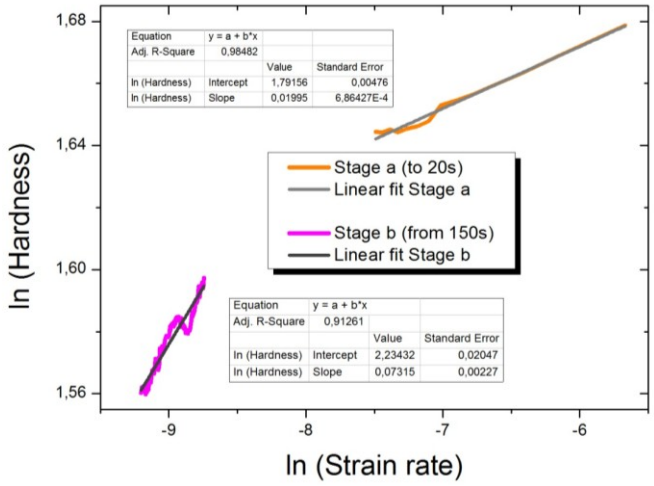

Fig. 4.49: Calculation through linear fitting curves (grey lines) of the strain rate sensitivity for Stage a (orange curves) and Stage b (magenta curves).

In the Fig. 4.50 to Fig. 4.56 the ln(Hardness) over ln(Strain rate) curves are shown for each temperature (equation 2.6). The obtained strain rate sensitivities for the two stages are clearly pointed out. The data was standardised in order to avoid a high scatter of the curves.

<u>Results of the first experimental run</u>

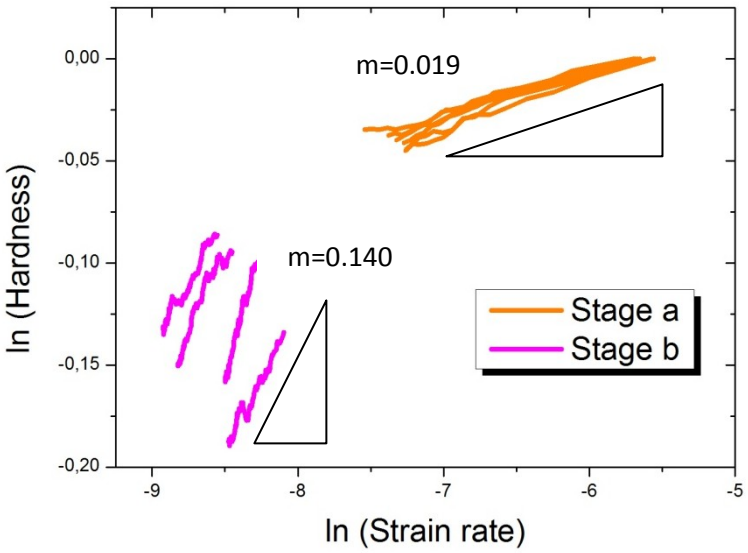

Fig. 4.50: Strain rate sensitivity data in a ln (Hardness) over ln (Strain rate) plot for room temperature; Stage a (orange) and Stage b (magenta) are pointed out.

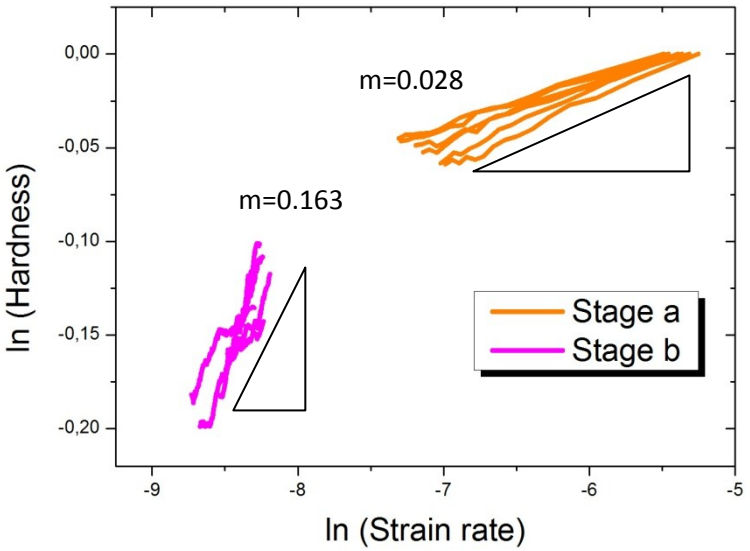

Fig. 4.51: Strain rate sensitivity data in a ln (Hardness) over ln (Strain rate) plot for 100 °C; Stage a (orange) and Stage b (magenta) are pointed out.

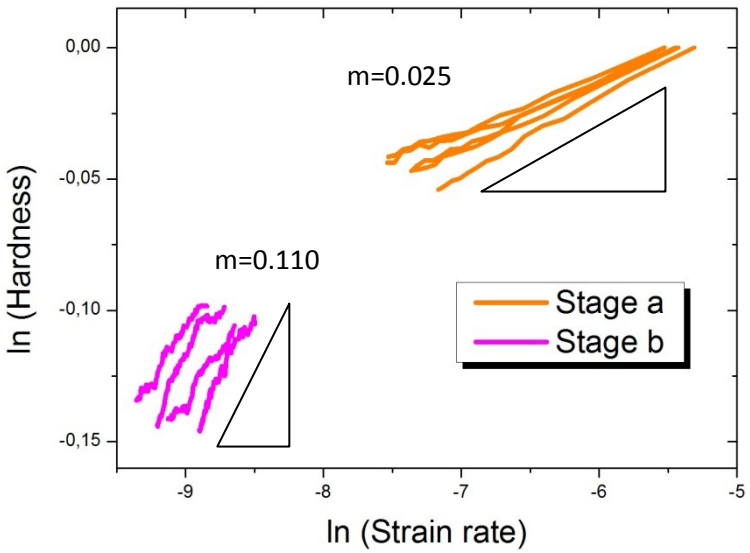

Fig. 4.52: Strain rate sensitivity data in a ln (Hardness) over ln (Strain rate) plot for 200 °C; Stage a (orange) and Stage b (magenta) are pointed out.

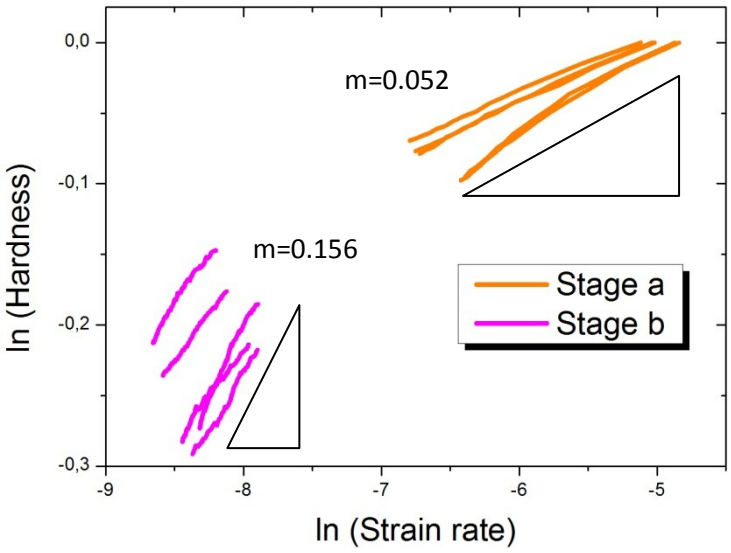

Fig. 4.53: Strain rate sensitivity data in a ln (Hardness) over ln (Strain rate) plot for 300 °C; Stage a (orange) and Stage b (magenta) are pointed out.

Results of the second experimental run

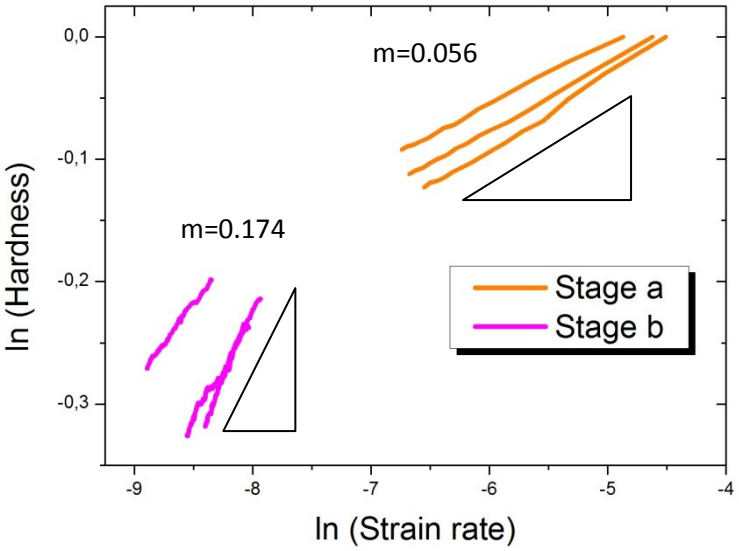

Fig. 4.54: Strain rate sensitivity data in a ln (Hardness) over ln (Strain rate) plot for 300 °C; Stage a (orange) and Stage b (magenta) are pointed out.

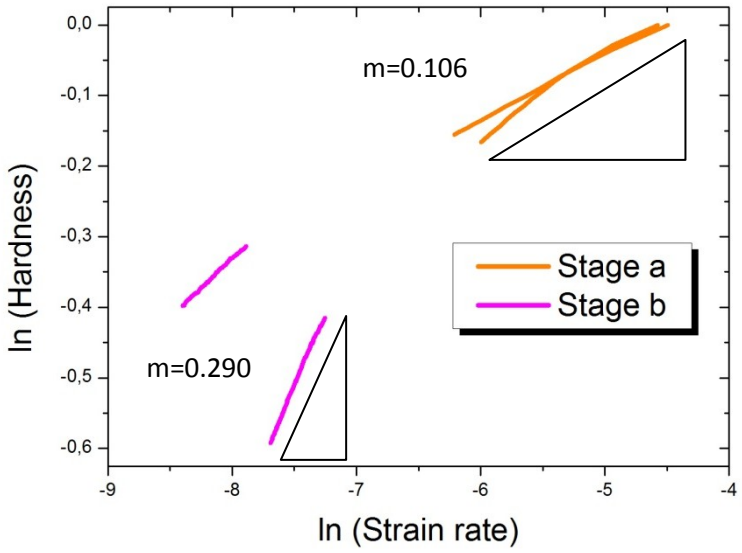

Fig. 4.55: Strain rate sensitivity data in a ln (Hardness) over ln (Strain rate) plot for 400 °C; Stage a (orange) and Stage b (magenta) are pointed out.

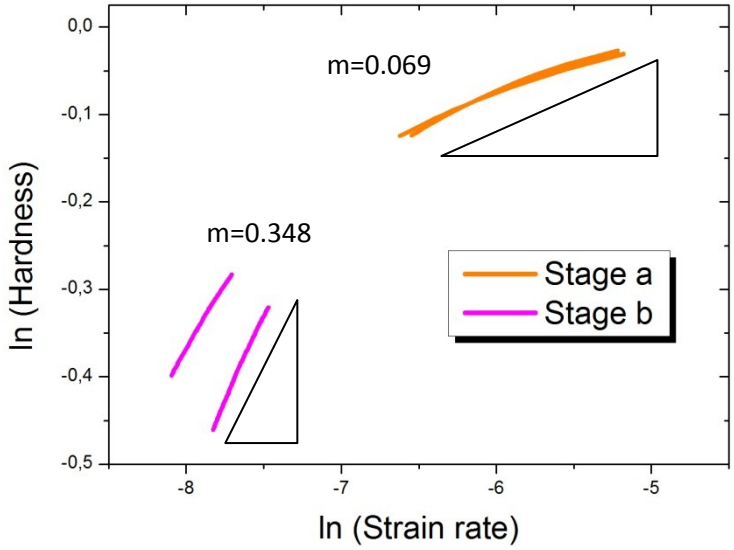

Fig. 4.56: Strain rate sensitivity data in a ln (Hardness) over ln (Strain rate) plot for 500 °C; Stage a (orange) and Stage b (magenta) are pointed out.

Fig. 4.57 shows the strain rate sensitivity values obtained from “stage a” and “stage b”. The difference between these two stages is obvious. The SRS values of “stage b” exhibit at elevated temperatures (400 °C and 500 °C) values in the range of 0.30. These values seem to be overestimated, due to the fact that at this temperatures (homologous temperature of approximately 0.5 in the case of copper; smaller than 0.3 in the case of niobium) no diffusion

process should occur. For this reason, the values obtained from “stage b” should not be further investigated.

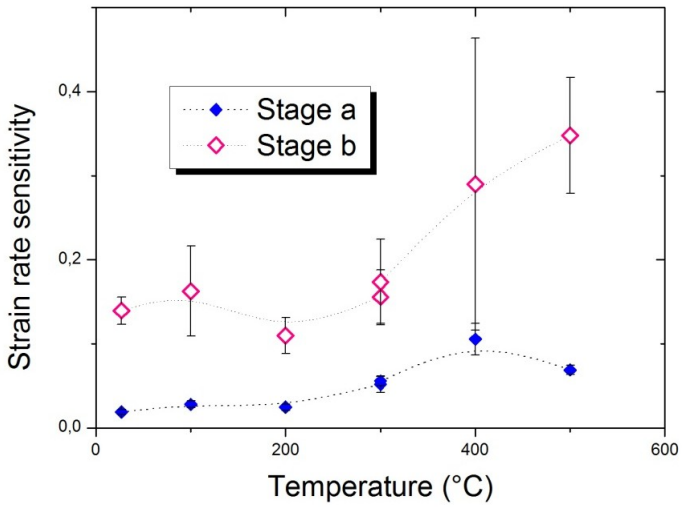

Fig. 4.57: Strain rate sensitivity as a function of temperature; “stage a” and “stage b”.

In Fig. 4.58 the strain rate sensitivity values for “stage a” are shown. At the first testing temperatures (room temperature to 200 °C) the copper niobium composite exhibits lower SRS values than at elevated temperatures (above 300 °C). The SRS value at room temperature is approximately 0.019, which is in accordance with several previous observed values for nc materials, e.g. copper or similar Cu Nb composites, as will be discussed later in this chapter.

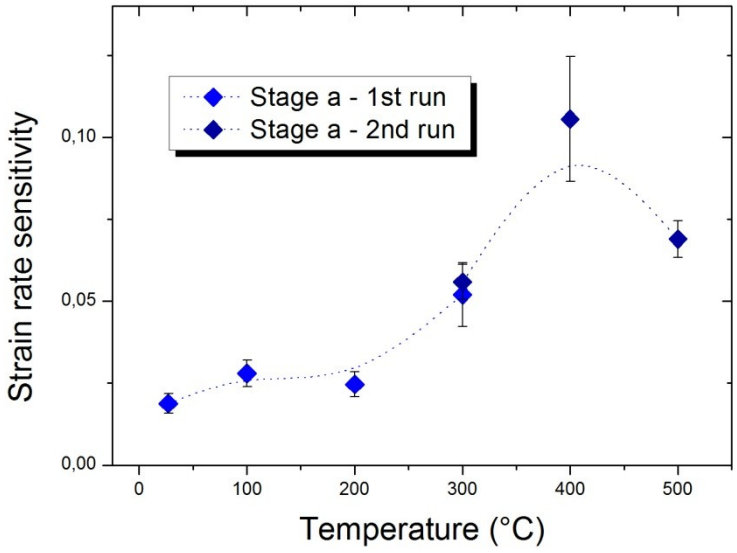

Fig. 4.58: Strain rate sensitivity as a function of temperature; “stage a”.

In order to avoid the “hump” seen in Fig. 4.58, in one case the SRS value at 500 °C is assumed to be an outlier (a graphic account can be seen in Fig. 4.59) and in the other case the value at 400 °C is assumed to be an outlier (as shown in Fig. 4.60). To obtain a smoothed curve, once the value obtained at 500 °C and respectively another time at 400 °C was not included for further discussion. In Fig. 4.59 and Fig. 4.60 the strain rate sensitivities as a function of temperature are shown.

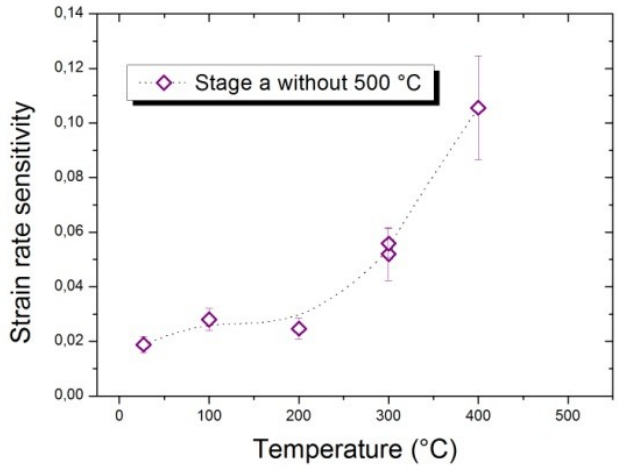

Fig. 4.59: Strain rate sensitivity as a function of temperature; 500 °C result is an outlier.

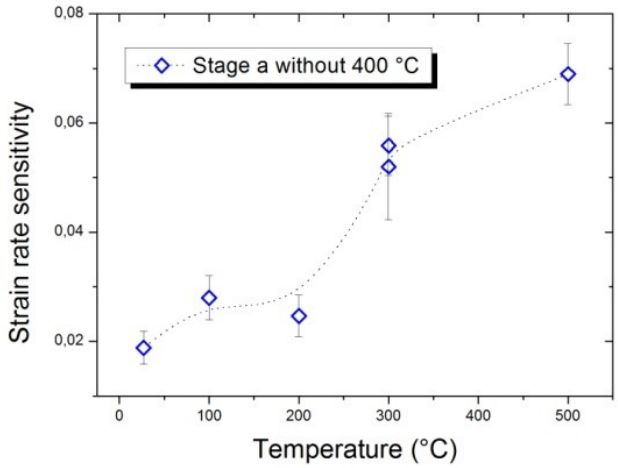

Fig. 4.60: Strain rate sensitivity as a function of temperature; 400 °C result is an outlier.

In previous investigations [29] and [30] a higher value of the strain rate sensitivity m was observed when reducing the grain size down to ufg and nc regime for fcc metals as can be seen in Fig. 4.61 and Fig. 4.62 for copper. In both figures a transition region is apparent, ap-

proximately at the beginning of the ufg range (d = 500 nm). From this transition grain size the m value rises significantly to higher strain rate sensitivities for nc materials.

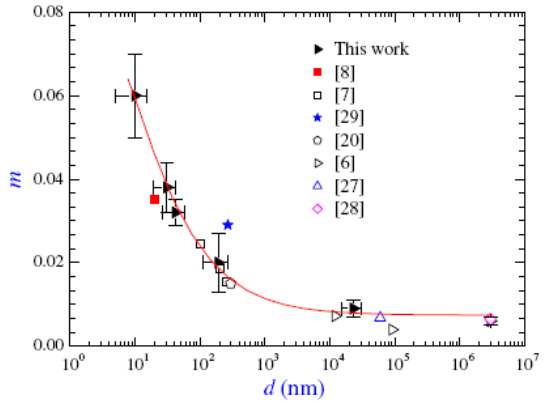

Fig. 4.61: Increase of the strain rate sensitivity with decreasing grain size d [29].

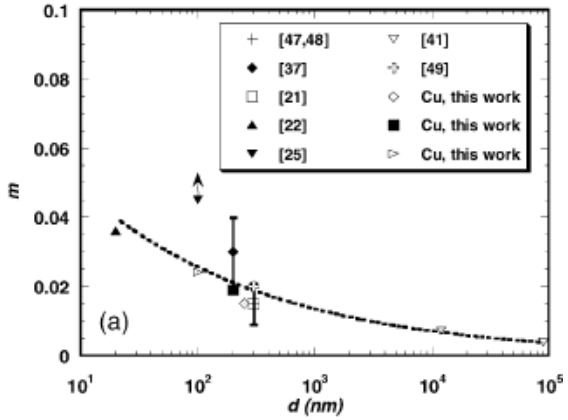

Fig. 4.62: Increase of the strain rate sensitivity with decreasing d in fcc metals [30].

An opposite trend was observed for bcc metals, according to Fig. 4.63. With decreasing the grain size, the SRS values are getting lower. Furthermore there is no “take-off” in the ufg area apparent, as could be seen in Fig. 4.61.

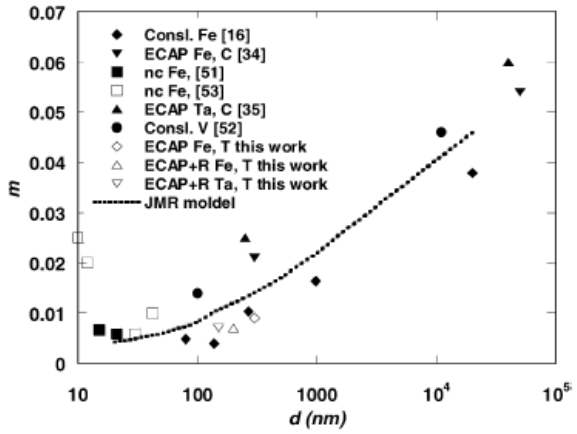

Fig. 4.63: Decrease of the strain rate sensitivity with decreasing grain size in bcc metals [30].

The strain rate sensitivity as a function of temperature to a maximum of 300 °C for nc nickel (Fig. 4.64) and ufg copper (Fig. 4.65) are shown. According to the investigations of the fcc element nickel a huge difference between a conventional cg material and the nc counterpart in the SRS is obvious. Furthermore the increase over temperature is much higher in the nc sample than in the conventional sample. The data of the nc Ni shows a quadratic trend.

The values at room temperature and in the case of elevated temperatures to 300 °C of the nc Cu exhibit a similar trend as was obtained in this work. At room temperature and at elevated temperatures (100 °C and 200 °C) Tao et al. [25], obtained slightly higher values 0.02, whereas almost the same values were observed in this work. What is more an increase to a SRS of approximately 0.05 was observed in both cases for 300 °C. Because of this similarity it was assumed, that the SRS value at 500 °C is an outlier and hence should be discarded.

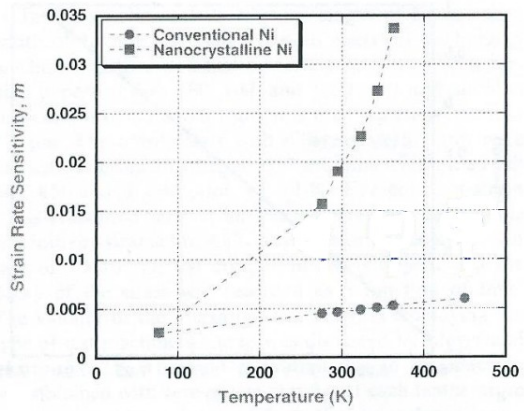

Fig. 4.64: Strain rate sensitivity over temperature for nc Ni compared to cg Ni [31].

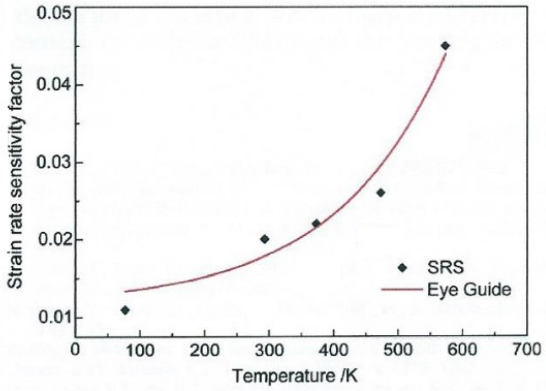

Fig. 4.65: Temperature dependence of the strain rate sensitivity for ufg Cu [25].

4.3.5 Activation volume

In order to determine the governing deformation mechanism of the copper niobium composite at each temperature the activation volume was calculated with equation 2.8 from chapter 2.2. A logarithmic diagram of the activation volume can be seen in Fig. 4.66.

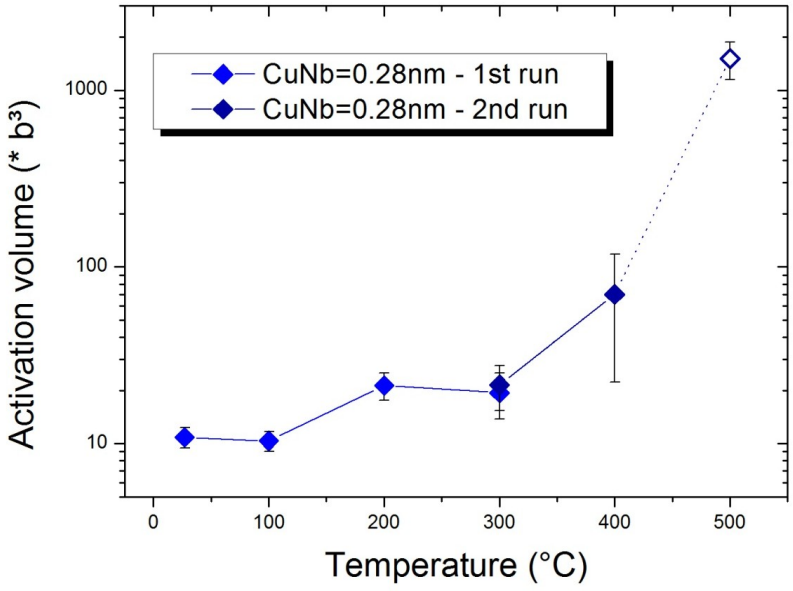

Fig. 4.66: Activation volume for a Burger's vector of b = 0.28 nm.

The Burger's vector (b) was set to b = 0.28 nm according to a rule of mixture calculation by Zhu et al. [32]. The curve exhibits a slight increase of the activation volume to a temperature of 300 °C – V* around $10 \cdot b^3$ to $20 \cdot b^3$. An overlapping of the values from the first and the second experimental run is obvious. The activation volume shows at 400 °C approximately three times higher values, approximately $70 \cdot b^3$, than at prior temperatures. At 500 °C the activation volume rises again more than 15 times higher compared to prior temperatures to approximately $1100 \cdot b^3$.

For coarse grained materials the deformation mechanisms are well investigated. In Table 4.18 the plastic deformation mechanism as well as a rough estimation of the corresponding order of the activation volume is represented.

Table 4.18: Activation volume and corresponding deformation mechanism

Deformation mechanism	Order of magnitude
Dislocation interaction	$> 10^3 \cdot b^3$
Grain boundary	$10^1 - 10^2 \cdot b^3$
Diffusion	$10^0 - 10^1 \cdot b^3$

The Table 4.18 is only valid for cg materials; otherwise the governing deformation mechanisms of the copper niobium composite would be at lower temperatures diffusion processes and at higher temperatures dislocation interactions. According to previous observations, for example [29], the activation volume decreases with decreasing the nominal grain size of the material, whereas the governing deformation mechanism, in this case dislocation interaction, remains the same. The decrease of the activation volume with a decrease in the grain size is shown for copper in Fig. 4.82 from [29].

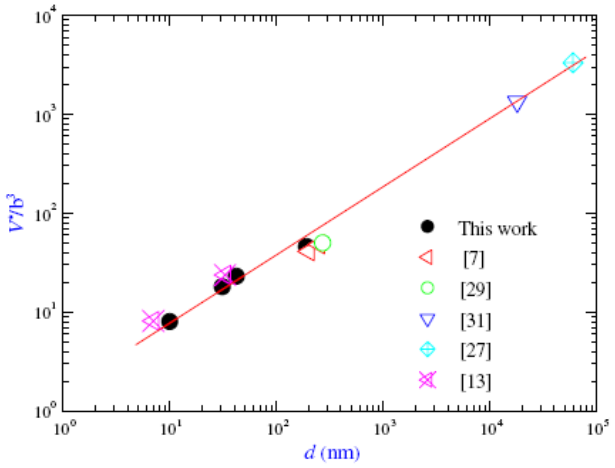

Fig. 4.82: Activation volume V* in dependence of the grain size d for nc Cu [29]

The copper niobium composite has a nominal grain size of approximately 200 nm and has a activation volume at room temperature of approximately $10 \cdot b^3$. In accordance with Fig. 4.82 the governing deformation mechanism is assumed to be a dislocation interaction with (sub-) grain boundaries at room temperature. This was also proposed for nc Cu in [30].

At elevated temperatures (from 100 °C to 300 °C) the activation volume stays nearly constant, indicating no significant changes in the deformation mechanism and hence in the microstructure of the composite. The dislocation interaction with (sub-) grain boundaries is still apparent.

At higher temperatures (400 °C and 500 °C) the values of the activation volume are getting higher and higher. According to Fig. 4.82 it is assumed that grain growth occurs. This assumption would explain the rising values of the strain rate sensitivity. The activation volume is rising due to the fact that the governing plastic deformation mechanism has changed slightly. The deformation is still governed by dislocation interaction, but the obstacles to glissile dislocations are not longer grain boundaries, but forest dislocation [30].

5 Summary

5.1 General discussion

In general, composites are promising engineering materials for prospective purposes in various fields, ranging from applications in medicine to the energy technology. It is well known that a decrease of the structure size of a material to the nano-regime (nano-crystalline and ultrafine grain range) results for example in a higher hardness, improved ductility or in better physical properties. For this reason it is evident that combining a composite material with a structure size down to the nc or ufg regime should possess outstanding properties.

In previous investigations it was shown that bcc / fcc composites in the nc / ufg range exhibit such outstanding properties in various fields. One of these composites is the compound material assembled by the fcc element copper and the bcc element niobium. Copper niobium composites have shown a broad spectrum of possible fields of application depending on the manufacturing route and/or the exact composition of the material, for example [2, 5].

One of the possible applications is in the energy technology; to be more precise as a structural material in nuclear reactors. It was proposed in several previous investigations that a copper niobium composite exhibits a high radiation tolerance [8, 9] and thermal stability after heat treatments [4, 5, 6]. These two mentioned properties are optimal requirements for the use in harsh circumstances, as it is given in nuclear reactors.

In this work a severe plastic deformation processing route, the “two step” HPT process, was used to create a copper niobium composite in the ufg regime. The composite exhibits a fine microstructure, even after a heat treatment at 500 °C for 60 minutes, in the range of approximately 100 to 200 nm and shows over approximately 800 µm constant microhardness values. This area was needed for further nanoindentation measurements.

Several significant mechanical properties as a function of temperature were investigated in-situ using high temperature instrumented indentation techniques. The maximum testing temperature was limited to 500 °C. With this nanoindentation tests it was possible to investigate basic properties of the material – e.g. the hardness and the elastic modulus – as a function of temperature in order to estimate the maximum operating temperature for the composite. Furthermore the governing deformation mechanism over operating temperatures could be determined with two parameters – the strain rate sensitivity and the activation volume of the flow stress.

5.2 Detailed discussion

The hardness as a function of temperature is shown in Fig. 5.1. At room temperature and 100 °C the hardness exhibits high values compared to other copper niobium composites as was shown in chapter 4.3.2. According to [33] structural materials (in this case nickel-base alloys) for nuclear engineering purposes should exhibit a 0.2 % proof stress of approximately 250 MPa at 100 °C and 170 MPa at 400 °C.

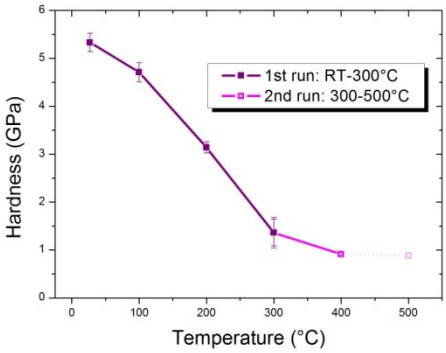

Fig. 5.1: Hardness as a function of temperature from the first and the second run

The copper niobium composite exhibits even at elevated temperatures around 300 °C a hardness of approximately 1.2 GPa and hence a ultimate tensile strength of approximately 0.4 GPa or 400 MPa. According to the obtained results and the recommendation for structural materials for nuclear purposes from BÖHLER Edelstahl [33] the material offers good characteristics when hardness and strength are considered. The maximum operating temperature of the copper niobium composite is approximately at 300 °C.

The second important mechanical property, the elastic modulus, was also determined as a function of temperature. In Fig. 5.2 and Fig. 5.3 the data for the Young's modulus is shown.

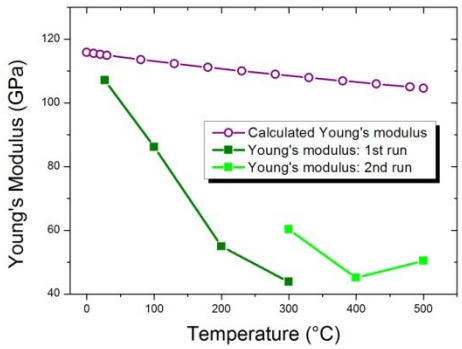

Fig. 5.2: Young's modulus compared to the calculated modulus of the composite

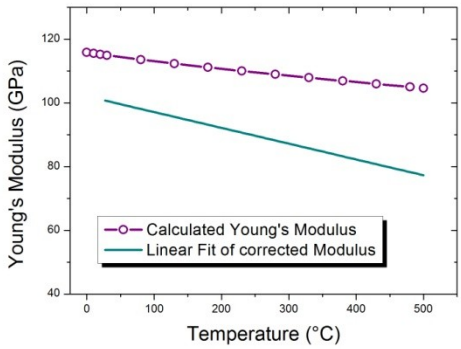

Fig. 5.3: Fit of corrected modulus compared to the calculated modulus of the composite

As was discussed before in chapter 4.3.3, a few assumptions had to be made when analysing the elastic modulus. The obtained values from the measurements can be seen in Fig. 5.2, in Fig. 5.3 the corrected elastic modulus of the composite (blue curve) is compared to the calculated Young's modulus of the copper niobium composite. It is assumed that the modulus exhibits a decrease of approximately 20 % from room temperature to 500 °C.

The strain rate sensitivity (Fig. 5.4 and Fig. 5.5), as well as the activation volume of the flow stress (Fig. 5.6), was investigated in order to determine the governing deformation mechanism at elevated temperatures.

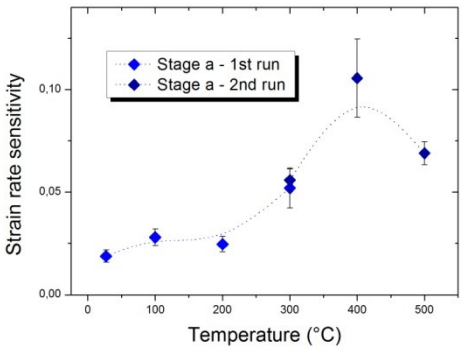

Fig. 5.4: Strain rate sensitivity as a function of temperature; Stage a from CL tests

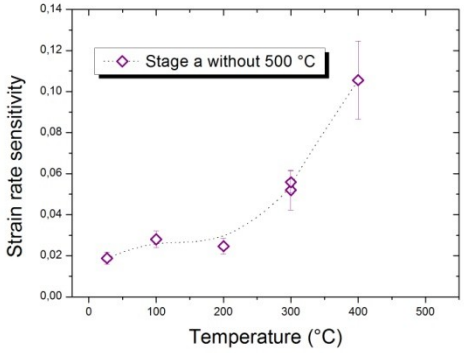

Fig. 5.5: Corrected strain rate sensitivity as a function of temperature; without 500 °C

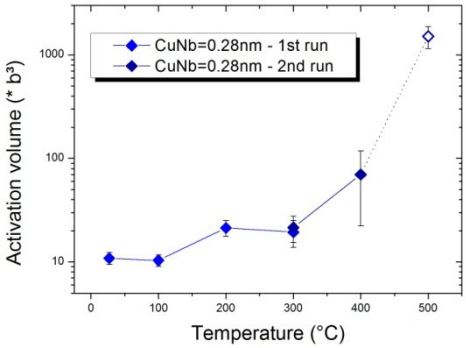

Fig. 5.6: Activation volume as a function of temperature

The SRS measurements showed an increase in the dependence of strain rate especially at higher temperatures of 400 °C. It is proposed that the deformation mechanism does not change at higher temperatures at is defined by a dislocation interaction. At low temperatures (from room temperature to approximately 300 °C) the obstacles for dislocation motion are the (sub-) grain boundaries; at elevated temperatures (above 400 °C) forest dislocation prevent the motion of glissile dislocations.

6 Literature

[1] "Chemsoc periodic table," 2013. [Online]. Available: http://chemsoc.velp.info/. [Accessed 12 August 2013].

[2] E. Botcharova et al., "Supersaturated solid solution of niobium in copper by mechanical alloying," *Journal of Alloys and Compounds 351,* pp. 119-125, 2003.

[3] E. Botcharova et al., "Mechanical alloying of copper with niobium and molybdenum," *Journal of Materials Science 39,* pp. 5287-5290, 2004.

[4] E. Botcharova et al., "High thermal stability of mechanically-alloyed nanocrystalline Cu-Nb alloys," *Int. J. Mat. Res. 97,* pp. 1350-1354, 2006.

[5] A. Misra et al., "Effects of elevated temperature annealing on the structure and hardness of copper/niobium nanolayered films," *J. Mater. Res., Vol. 20, No. 8,* pp. 2046-2054, Aug 2005.

[6] N. Mara et al., "High-temperature mechanical behavior/microstructure correlation of Cu/Nb nanoscale multilayers," *Materials Science and Engineering A 493,* pp. 274-282, 2008.

[7] N. Mara et al., "Tensile behavior of 40 nm Cu/Nb nanoscale multilayers," *Scripta Materialia 58,* pp. 874-877, 2008.

[8] X. Zhang et al., "Nanostructured Cu/Nb multilayers subjected to helium ion-irradiation," *Nuclear Instruments and Methods in Physics Research Section B: Beam Interactions with Materials and Atoms, Volume 261, Issues 1–2,* pp. 1129-1132, 2007.

[9] N. Li et al., "Defect structures and hardening mechanism in high dose helium ion implanted Cu and Cu/Nb multilayer thin films," *International Journal of Plasticity, Volumes 32-33,* pp. 1-16, 2012.

[10] M. Meyers et al., "Mechanical properties of nanocrystalline materials," *Progress in Materials Science 51,* pp. 427-556, 2006.

[11] I. Sabirov et al., "Fabrication of a W-25%Cu nanocomposite by high pressure torsion," *Materials Science Forum, Volumes 503-504,* pp. 561-566, 2006.

[12] A. Bachmeier et al., "The formation of supersaturated solid solutions in Fe-Cu alloys deformed by high-pressure torsion," *Acta Materialia 60,* pp. 860-871, 2012.

[13] A. C. Fischer-Cripps, Introduction to Contact Mechanics, 2nd ed., New South Wales: Springer, 2007, pp. 189-198.

[14] V. Maier, "PhD thesis, University of Erlangen-Nurnberg, Erlangen-Nurnberg," 2013.

[15] M. Mayo et al., "A micro-indentation study of superplasticity in Pb, Sn, and Sn-38 wt% Pb," *Acta Metallurgica, Volume 36, Issue 8,* pp. 2183-2192, 1988.

[16] J. Alkorta et al., "Critical examination of strain-rate sensitivity measurement by nanoindentation methods:

Application to severely deformed niobium," *Acta Materialia, Volume 56, Issue 4,* pp. 884-893, 2008.

[17] V. Maier et al., *J. Mater. Res. 26,* p. 1421, 2011.

[18] B. Lucas, "PhD Thesis, University of Tennessee, Knoxville," 1997.

[19] B. Lucas et al., *Metall Mater Trans A 30,* p. 601, 1999.

[20] M. Mayo et al., *J. Mater. Res. 5,* p. 1073, 1990.

[21] M. Mayo et al., *J. Mater. Res. 7,* p. 973, 1992.

[22] D. Peykov et al., "Evaluation of strain rate sensitivity by constant load nanoindentation," *J. Mater. Sci. 47,* pp. 7189-7200, 2012.

[23] A. Vorhauer et al., "On the homogeneity of deformation by high pressure torsion," *Scripta Materialia, Volume 51, Issue 9,* pp. 921-925, 2004.

[24] B. Farrokh et al., „Grain size, strain rate, and temperature dependence of flow stress in ultra-fine grained and nanocrystalline Cu and Al: Synthesis, experiment, and constitutive modeling," *International Journal of Plasticity,* pp. 715-732, 2009.

[25] S. Tao et al., "Experimental investigation on strain rate sensitivity of ultra-fine grained copper at elevated temperatures," *Mechanics of Materials 43,* pp. 111-118, 2011.

[26] R. Carreker et al., „Tensile deformation of high-purity copper as a function of temperature, strain rate, and grain size," *Acta Metallurgica 1,* pp. 654-663, 1953.

[27] "WebElements periodic table," 2013. [Online]. Available: http://www.webelements.com/. [Accessed 12 August 2013].

[28] G. Simmons et al., "Single Crystal Elastic Constants and Calculated Aggregate Properties," Cambridge, Massachusetts, and London, England, The MIT Press, pp. 178-233.

[29] J. Chen et al., "Hardness and strain rate sensitivity of nanocrystalline Cu," *Scripta Materialia 54,* pp. 1913-1918, 2006.

[30] Q. Wei et al., "Effect of nanocrystalline and ultrafine grain sizes on the strain rate sensitivity and activation volume: fcc versus bcc metals," *Materials Science and Engineering A 381,* pp. 71-79, 2004.

[31] Y. Wang et al., "Temperature-dependent strain rate sensitivity and activation volume of nanocrystalline Ni," *Acta Materialia 54,* pp. 2715-2726, 2006.

[32] X. Zhu et al., „Microstructure and ultrahigh strength of nanoscale Cu/Nb multilayers," *Thin Solid Films 520,* pp. 818-823, 2011.

[33] "Boehler Edelstahl," 2013. [Online]. Available: http://www.bohler-edelstahl.com/files/L276DE.pdf. [Accessed 12 August 2013].